Received: 3 November 2022 | Revised: 24 July 2023 | Accepted: 3 August 2023

DOI: 10.1002/arp.1910

RESEARCH ARTICLE

WILEY

A novel seismic full waveform inversion approach for assessing the internal structure of a medieval sea dike

Michaela Schwardt | Dennis Wilken | Daniel Köhn | Wolfgang Rabbel

Department of Geophysics, Institute of Geosciences, Kiel University, Kiel, Germany

Correspondence
Michaela Schwardt, Department of Geophysics, Institute of Geosciences, Kiel University, Otto-Hahn-Platz 1, 24118 Kiel, Germany.
Email: michaela.schwardt@ifg.uni-kiel.de

Funding information
Deutsche Forschungsgemeinschaft, Grant/Award Number: RA 496/26-2

Abstract

Coastal protection in the form of dike constructions has a long history at the German North Frisian coast dating back to the High Middle Ages. As the vast majority of the dikes built prior to the devastating storm surges of the Middle Ages have been irretrievably destroyed, mostly sparse remains and only a few well preserved of these medieval dikes are found along the German North Frisian coast and within the Wadden Sea. Not all details of their construction and dimensions are yet understood. In the present case study, we investigate the historical Schardeich on the island of Pellworm in the German North Sea in a noninvasive way using shear waves (SH-waves). For the data interpretation, we applied a combination of seismic full waveform inversion and classical seismic reflection imaging to determine the interior structure of the dike and its underlying layers at the highest possible resolution. The results obtained on land are compared with dike remains found in the tidal flats. These remains show up in marine seismic sections as characteristic reflections, which probably represent a compaction layer caused by the load of the former dike. For ground truthing, we compare the seismic results with internal dike structures found in nearby excavations. The comparison highlights that FWI is a reliable tool for near-surface archaeological prospecting. We find that SH-wave FWI provides decimetre-scale velocity and density models that allow, together with the seismic reflection section, to determine distinct construction phases of the dike. The investigated dike further shows a depression at base level of about 0.75 m, which is of the same order as observed for the dike base reflections in the tidal flats. Transferring these findings to the dike remains mapped in the tidal flats, we derive a height of the former dike from 2.2 to 4.4 m.

KEYWORDS
archaeogeophysics, high-resolution seismic reflection imaging, seismic full waveform inversion, shear-wave seismic

1 | INTRODUCTION

In times of threatening rising sea levels due to climate change, the importance of coastal and landscape protection is of increasing importance. Yet, coastal protection in the form of dike constructions already has a long history at the German North Frisian coast and began in the High Middle Ages. Since then, dikes have been indispensable for the protection of land and population, as well as for land reclamation,

because storm surges and varying sea levels have shaped the coastline before the beginning of its settlement history (e.g., Bantelmann & Fischer, 1967; Hadler, Vött, et al., 2018; Meier, 2007).

The history of the German North Frisian Wadden Sea demonstrates that historical dike construction has been a dynamic process and continuous adaptations to new conditions have been necessary. Although several historic dikes of different ages, heights and designs can be found along the German North Sea coast, especially on the Eiderstedt Peninsula (Bauer et al., 2001; Meier, 2007; Muuß, 1927) not all details of the historical dike construction are yet understood as the vast majority of the dikes built prior to the devastating storm surges of 1362 (Marcellus Flood; 1st Grote Mandrenke) and 1634 (Burchadi Flood; 2nd Grote Mandrenke) have been irretrievably destroyed and only remnants are found in some areas. Excavations would allow conclusions to be drawn about these dikes, provided they are nowadays located on land. However, by far the greater part of the historical cultural landscape is located within today's tidal flats, often covered by several metres of sediment. These circumstances do not allow excavation of the structures and traces of settlements can only be mapped if they are exposed. Nevertheless, one possible method of mapping remnants in this area are geophysical surveys, which allow the investigation during both low and high tides (e.g., Hadler, Vött, et al., 2018; Wilken et al., 2022).

One example of the successful mapping of dikes and other settlement traces has been done by Busch in 1921 on the tidal flats in the so-called Rungholt area near the Hallig of Südfall (Busch, 1936, 1960; Meier, 2007). Today, about 100 years later, these remnants are covered by up to 1.5 to 2.0 m thick recent tidal flat deposits (e.g., Hadler, Vött, et al., 2018; Hadler, Wilken, et al., 2018) and were recently investigated by Wilken et al. (2022), who performed geophysical and geoarchaeological investigations, revealing large parts of a medieval dike system by magnetic gradiometry. Complemented by seismic reflection profiles to gain depth resolving insights into the remaining dike structures, they found that only a small fraction of the dike may still be present. In most cases, however, depression-shaped seismic reflectors can be seen at the expected position of the dike, indicating subsoil layers of fossil marsh and organic mud deposits that have been deformed by the load of the dike. This deformation is referred to as dike steel (German "Deichstahl"; Newig & Petersen, 1995). Despite the findings of the mentioned studies, little is known about these dikes, especially in terms of their dimensions.

Concerning the remnants of the dike system, the question therefore arises how conclusions about the dimensions of the dikes can be drawn from geophysical investigations, in particular from depth resolving methods such as seismic reflection profiling. Fortunately, there are still some dikes of similar age found along the North Frisian coast that can be geophysically investigated for comparison. One example is the so-called "Schardeich" located on the island of Pellworm on which we focus in this study (Figure 1). It is of the same age as the aforementioned dike remains in the nearby tidal flats. While potential field methods such as electric resistivity tomography (ERT) are used for the investigation of mainly modern dikes, seismic methods play a minor role as they usually do not meet the resolution requirements despite their good penetration depth (e.g., Bièvre & Norgeot, 2005; Fauchard & Mériaux, 2007; Jaksch, 2009; Niederleithinger et al., 2012). However, as has been shown by several previous studies, seismic full waveform inversion (FWI) is a promising tool in near surface geophysical investigation and is able to provide detailed velocity and density models of the subsurface (e.g., Köhn et al., 2019; Mecking et al., 2021; Rusch et al., 2022; Schwardt et al., 2020) as it increases the seismic resolution allowing to image objects smaller than the seismic wavelength (e.g., Dokter et al., 2017). Therefore, through the application of advanced seismic methods like FWI, a high-resolution image of the interior structure of the dike and underlying layers can be anticipated. So-called ground truthing is possible; that is, the results obtained by means of geophysical investigations can be directly compared with the internal structure of the dike known from excavations (Kühn, 1989, 1992; Kühn & Panten, 1989). This work focuses on the following objectives:

1. From a methodological point of view: Are the applied seismic methods capable of imaging the internal structure of the dike as known by the available excavation?
2. Does the investigated dike have a footprint similar to that seen for the remnants in the nearby tidal flats?
3. From an archaeological point of view: Can conclusions be drawn about the dimensions of the dike, mainly based on the geophysical image of the footprint?

To answer these questions, we applied FWI along with seismic reflection profiling to the well investigated Schardeich on the island of Pellworm. We focused on seismic methods to ensure a comparability with the results for the dike remains in the nearby tidal flats obtained by Wilken et al. (2022). Similar to Schwardt et al. (2020), who emphasized the use of a combined FWI-reflection section for a better understanding of reflections and thus allowing better interpretation, we present a combined model of seismic reflections and FWI-based velocity and density models.

This paper is structured as follows: After a brief description of the measurement site including a short geological-historical overview in Section 2 and a description of the methodology in Section 3, the results are described, classified and discussed with respect to the key questions in Sections 4 and 5. Finally, a conclusion and an outlook are provided.

2 | THE SITE: LOCATION, HISTORY AND PREVIOUS RESEARCH

2.1 | Research area

Today, the coastal area of North Frisia (Figure 1a) extends from the Eiderstedt peninsula in the south to the German-Danish border in the north. In the southern part of the North Frisian Wadden Sea two larger marshland islands, Pellworm and Nordstrand, and many smaller islands, the so-called "Halligen" are located (Meier, 2004). These

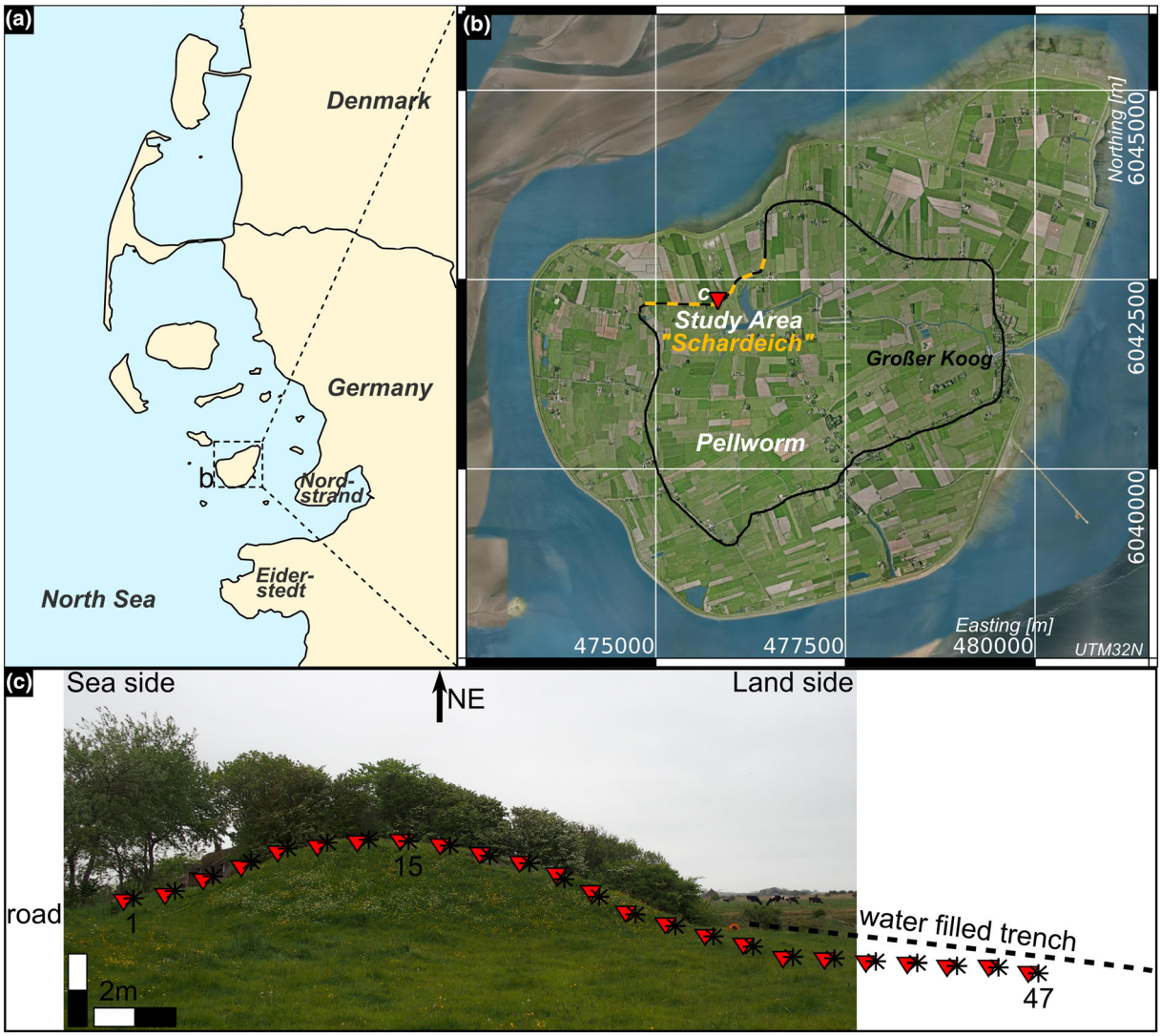

FIGURE 1 Maps of the study site showing the German North Frisian coast from the Eiderstedt Peninsula in the South to the German-Danish border in the North (a), and the island of Pellworm with the location of the Schardeich marked with a dashed yellow line. The Großer Koog is surrounded by a black line, a red triangle marks the location of the seismic investigations (b). Photograph of the remaining Schardeich (c) looking in North-eastern direction. The positions of every second geophone and shot point are indicated by black asterisks and red triangles, respectively. Not pictured in the photograph are the road located to the North (left in the photograph) and the water filled trench located to the South (right in the photograph). Photograph taken by M. Schwardt.

islands have endured the devastating floods of the Medieval and Modern periods and many cultural traces still bear witness to the history of medieval settlement.

The dike on which we focus in this study, the so-called "Schardeich," is located on the island of Pellworm (Figure 1b). It surrounds the Großer Koog and is the oldest dike found on the island of Pellworm, having survived the 1st Grote Mandrenke of 1362 (Meier, 2007). It probably served as a "Mitteldeich" (middle dike; second dike line) between the Großer Koog and the Wester Neuen Koog before 1634 and as a sea dike after the flood of 1634 until 1637, when new land could be reclaimed (Meier, 2007; Müller-Wille et al., 1988). Because it has no longer any protective function today, part of the dike has been removed in the 1970s. As a result of several excavations, this dike and its construction history is well documented and dated (Kühn, 1992). The seismic profile (Figure 1c) is located on the remaining section of the dike about 150 m northwest of the excavation documented by Kühn (1992).

2.2 | Geological and cultural history of North Frisia

With its coastal lowlands, diked marshlands and islands, the North Frisian coast is shaped by the tides and influenced by the sea like hardly any other landscape in the world. Over the centuries, the sea has repeatedly changed this landscape, thereby also influencing the cultural development and inhabitation. A detailed overview of the geological as well as cultural and settlement history since the last ice age is given by Meier (2007, 2008) and Hoffmann (2004), among

others. Not only the sea and natural disasters, but also anthropogenic utilization and cultivation since the Middle Ages have significantly contributed to today's appearance of the North Frisian coast, connecting the natural with the cultural history (e.g., Hadler, Wilken, et al., 2018). In particular, the more recent history of the coastline is linked to dike construction and land reclamation since the Middle Ages (Bantelmann & Fischer, 1967; Meier, 2007). Even today, humankind continues to play a formative role in shaping this coastal landscape (Hadler, Vött, et al., 2018).

Permanent settlement and cultivation of the marshland by Frisian settlers began at the end of the seventh to the beginning of the eighth century. Settlements were established on the natural land surface in the salt marshes on the elevated banks of tidal creeks (Meier, 2004, 2008). Rising sea levels forced the construction of terps and dikes to protect pastures, farmland and dwellings (Kühn & Panten, 1989; Meier, 2004, 2008). With the construction of dikes, the cultivation and inhabitation of low-lying areas became possible, thus soon transforming them from natural marshland into a cultivated landscape that was primarily used for agricultural purposes (Hadler, Wilken, et al., 2018; Kühn, 1992; Meier, 2004). However, the drainage of the diked marshland led to a subsidence of that land to a level below the mean high tide. Additionally, the dike building resulted in a reduction of the floodplains and consequently led to an increase of the tidal range as well as of the water heights during storm surges. As a result, the dikes had to be repeatedly raised, strengthened and thus adapted to the rising sea level since the 13th century (Hadler, Wilken, et al., 2018; Hoffmann, 2004; Meier, 2007, 2008; Newig, 2004). By the time the cultivation of marshland had reached its maximum extent in the 14th century, many coastal areas of North Frisia had already sunk below the level of the mean high tide revealing the significance of coastal protection by dikes (Hadler, Vött, et al., 2018; Hoffmann, 2004).

Since the end of the 13th century, severe storm surge events became more frequent (Meier, 2007). Far more than all later floods, the 1st Grote Mandrenke in 1362 shaped the North Frisian Uthlande: Many dikes were destroyed and within days considerable amounts of land were lost to the sea through extensive flooding, leading to a retreat of the coastline of about 25 km inland (e.g., Newig, 2004). In addition, the second Grote Mandrenke in 1634, in which the former island of Strand broke up into the islands of Pellworm and Nordstrand, essentially shaped today's coastline of North Frisia (Meier, 2007). The destruction of the dikes after both floods was followed by a rapid fragmentation of the marshland by tidal channels and its transformation into extensive mudflats. After 1634, attempts to re-dike the area of the old "Strand" were only successful on the island of Pellworm between 1635 and 1637 (Meier, 2007).

2.3 | Previous research conducted in this area

As the region has preserved a diverse cultural-historical heritage, it has been of importance for archaeological research. While a number of previous studies are primarily concerned with the geological development and its effects on the settlement history of the entire region, the area between the islands of Pellworm, Nordstrand and Südfall became of particular interest because of its high density of visible cultural traces such as plough marks or drainage ditches. Since the 1920s, Muuß (e.g., 1927) and Busch (e.g., 1936, 1960 and1963) have carried out extensive surveys and mapping of the remains. Although today the cultural traces are either eroded or covered by several metres of sediment, many remains could be mapped in the course of the Priority Program 1630 "Harbours from the Roman Period to the Middle Ages" (Von Carnap-Bornheim & Kalmring, 2011) by means of geophysical and geoarchaeological investigations (e.g., Hadler, Vött, et al., 2018; Hadler, Wilken, et al., 2018; Wilken et al., 2022).

3 | METHODOLOGY OF GEOPHYSICAL RESEARCH

3.1 | Data acquisition

One seismic shear wave profile across the historical dike on the Island of Pellworm was acquired (Figure 1c). SH-waves, that is, shear waves with a horizontal particle motion perpendicular to the profile direction, were excited by horizontal hammer blows against a steel plate that was coupled to the ground by steel spikes at its bottom; 48 horizontal-component 10-Hz geophones (10-Hz PE3 horizontal; Sensor), spaced 0.5 m apart with a maximum offset of 22.5 m, were used to record the seismic signals. The source points of the SH-waves were centred between each sensor. Both horizontal-component sensors and hammer blows were oriented perpendicular to the profile direction. At each excitation point, the signals of two hammer blows of the same polarization were recorded and stacked during processing to improve the signal-to-noise ratio (S/N). The same polarization has been chosen because there have been no P-waves recorded which needed to be eliminated. Figure 2a shows the shot gathers for three selected shots with an applied automatic gain control (AGC, window size 0.05 s) and a bandpass filter with cut-off frequencies of 10 and 100 Hz for visualization. Notice the distinct side reflections of the surface waves, caused by the adjacent road and a small water ditch on the left and right sides of the dike, respectively (see Figure 1c). The spectra are shown for three individual shots located at the sea side of the dike (shot no. 1; Figure 2b, left), at the top of the dike (shot no. 15; Figure 2b, middle) and at the end of the profile on the inland side (shot no. 47; Figure 2b, right). Figure 2c shows the corresponding averaged amplitude-frequency functions. The cumulative spectrum over all shots and the corresponding averaged amplitude-frequency function are displayed in Figure 2d. The raw data are shown in Figure A1 (Appendix A).

3.2 | Seismic data processing

In addition to a classical approach of reflection seismic processing described in Section 3.2.2, FWI is applied to determine detailed velocity and density models of the subsurface.

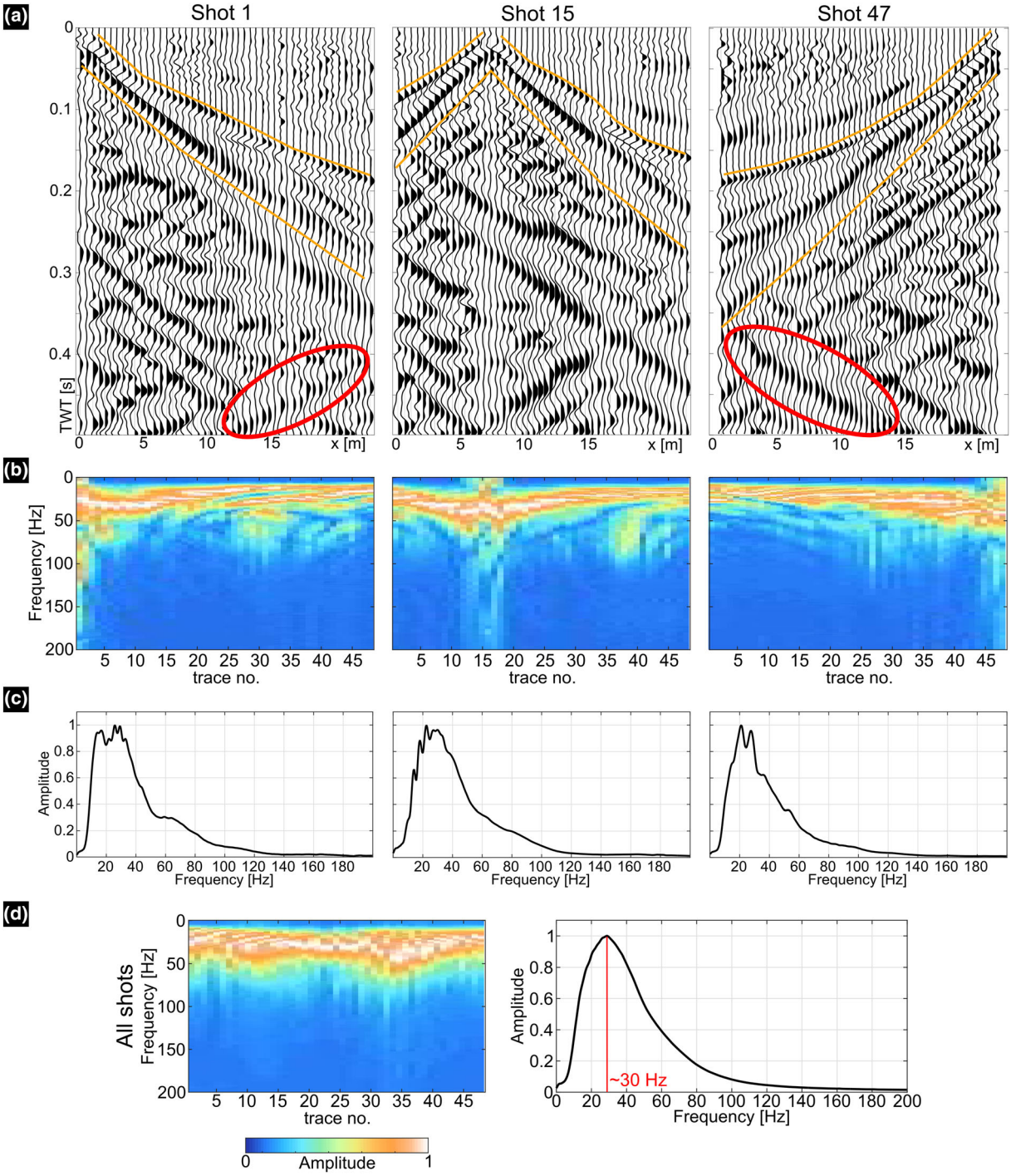

FIGURE 2 Shot gather (a), corresponding frequency spectra (b) and averaged amplitude-frequency functions (c) for three selected shots along the profile. In the shot gathers, the direct and surface waves are marked by an orange line. Red ellipses highlight exemplary side reflections from the water ditch (left, shot no. 1) and the adjacent road (right, shot no. 47). (d) The cumulative spectrum and the corresponding averaged amplitude-frequency function over all shots.

3.2.1 | 2D-SH seismic full waveform inversion

The FWI-code DENISE (Köhn et al., 2014) was applied for an inversion of the Love- and SH-wavefield in the time domain. The aim of the seismic 2D-SH FWI is the derivation of a high-resolution subsurface model of the physical parameters, namely, the horizontal shear wave velocity v_{SH} and the density distribution ρ by minimizing the misfit between the full wavefields of field and modelled data and fitting the model parameters. As all information of the seismic record is included in the inversion, that is both seismic phases and amplitudes, structures below the seismic wavelength can be resolved (e.g., Köhn et al., 2014; Mecking et al., 2021; Schwardt et al., 2020). For an overview of the

basic concepts of the applied FWI algorithm, we refer to, for example, Dokter et al. (2017), Köhn et al. (2014) and Appendix A.

Preprocessing of the seismic data (velocity; no instrument response removed) includes trace normalization to the maximum amplitude of each shot gather, the application of a time-dependent spreading correction to each shot gather (Forbriger et al., 2014) to compensate 3D spreading and point source effects, and resampling to a time step dt of $5{\cdot}10^{-5}$ s to meet the numerical stability conditions. In this case it is not necessary to remove the response for three reasons: (1) At frequencies smaller than 10 Hz, the signal transmission decays, but not abruptly, so there is still significant energy down to 5 or even 2 Hz which enters the computations; (2) at these low frequencies, the wavelength is greater than 20 m, which is very much larger that the target depth; (3) as the wavelet shape will be adjusted in the inversion process, phase shifts are not an issue. Further, we apply a time-delay of 0.05 s at the beginning of the seismic traces to avoid acausal parts during source wavelet estimation. As objective function during inversion, we use the trace normalized global correlation norm (GCN; eq. (1); after Choi & Alkhalifah, 2012), which previously has been successfully applied in other near-surface studies (e.g., Köhn et al., 2019; Rusch et al., 2022). The GCN is given by

$$E = -\sum_{i=1}^{ns}\int_0^T dt \sum_{j=1}^{nr}\left[\frac{u_{ij}^{mod}(t)\,u_{ij}^{obs}(t)}{\left\|u_{ij}^{mod}(t)\right\|_2\left\|u_{ij}^{obs}(t)\right\|_2}\right], \qquad (1)$$

where ns and nr are the number of shots and receivers, respectively, T is the recording time of the seismic data, $\|\cdot\|_2$ denotes the L2-norm and u_{ij}^{mod} and u_{ij}^{obs} are the modelled and observed data, respectively. The GCN, among other advantages (see Appendix B), puts a stronger weight on the seismic phase information compared with the amplitude information, thereby effects of varying amplitudes caused by, for example, insufficient receiver/source coupling are avoided (e.g., Dokter et al., 2017).

As the FWI is based on a local optimization approach, a starting point in the parameter space is necessary, which consists of initial models of SH-wave velocity v_{SH}, density ρ and damping factor Q_{SH}. The initial models are parameterized on a uniformly spaced 2D spatial Cartesian coordinate system with a grid spacing dh of 0.025 m. This very fine spatial discretization of the free surface of the pronounced topography of the dike is required to accurately model the Love wave propagation and dispersion with the Cartesian FD code within the framework of FWI. The initial shear-wave velocity model is adapted from the velocity model (Figure 3b) obtained by first arrival travel time tomography (FATT), which has been applied to the data using the program Reflexw by Sandmeier Geo (Sandmeier, 2004). The algorithm underlying the FATT as well as all parameters applied during the FATT are provided in Appendix C. The initial model is shown in Figure 3a. The final FATT velocity model (Figure 3b) is resampled to a grid spacing of $dh = 0.025$ m, extended to a total depth of 15 m, and smoothed by a 2D Gaussian filter to remove ray effects and small-scale details which could result in a convergence into side/local minimum. As only little prior information about the density was available, we use the empirical relation between the S-wave velocity and the density of Ulugergerli and Uyanik (2007), valid for near-surface soils, to estimate an initial density model, resulting in a density range of about 1800 to 1950 kg/m^3.

The initial velocity and density models for the FWI are shown in Figure B1 (Appendix B). For Q_{SH} a homogeneous half-space model is

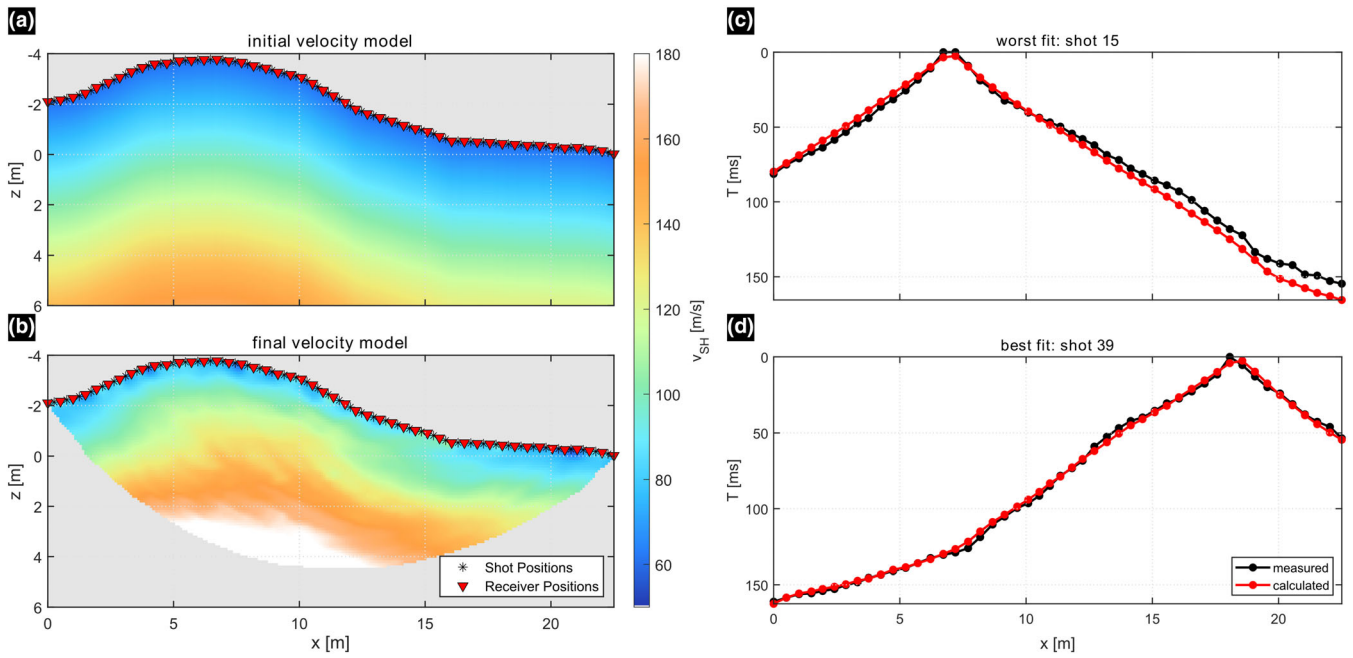

FIGURE 3 Initial (a) and final (b) velocity models of the applied FATT. On the right, a comparison between the measured (black dots) and the calculated (red dots) first arrival times is shown for the worst (c) and best (d) fitting shots. $Z = 0$ m equals NN, positive values denote a depth below NN.

assumed. To estimate the best value for Q_{SH}, we evaluated the seismogram fits and final objective functions after inversions with $Q_{SH} = 5$, 10, 15, 20 and 30. The best result with a minimal objective function value was obtained for $Q_{SH} = 5$, which fits well with literature values for the near surface sediments (e.g., Cox, 1999). During the inversion, the velocity and density models are inverted simultaneously, whereas the Q_{SH} model is not updated.

Besides an accurate initial model, the choice of the inversion strategy is essential for a successful application of the FWI (e.g., Köhn et al., 2019; Mecking et al., 2021). The inversion workflow has to be designed for the specific data set and acquisition geometry because of the nonlinearity of the inverse problem. On the basis of the work of Köhn et al. (2019), we applied a workflow consisting of the so-called LBL strategy, a sequential workflow of low-pass and band-pass filtered data with different bandwidths. This approach first optimizes low-pass filtered seismic data (L-step) with a sequentially increasing upper cut-off frequency, followed by an optimization of band-pass filtered data (B-step) with a fixed upper and sequentially increasing lower cut-off frequency. The last step consists of another optimisation of low-pass filtered data (L-step). For an overview of the cut-off frequencies, see Table B1 (Appendix B). While the first L-step allows an optimization of the dominating Love-wavefield, the B-step enhances the refracted SH-wavefield. The last L-step corrects a possible mismatch of the Love-wavefield caused by the second step. This inversion strategy results in an improved resolution and accurately fits the seismograms in terms of amplitudes and waveforms. The application of time and offsets windows as in Mecking et al. (2021) did not improve the final fit of the data. The FWI inversions were performed on the NEC-HPC Linux-Cluster at the computation centre of Kiel University, which consists of different Intel Xeon x86-64 cores. We used a total of 128 cores for each inversion. A full inversion run with about 100 Iterations took about 10–12 h on the cluster.

3.2.2 | Seismic reflection processing

The seismic reflection processing consists of several consecutive steps. Following the stacking of two shots of the same polarity to improve the S/N ratio, a spreading correction and trace normalization is applied. For visualization purposes we applied an AGC with a window length of 0.05 s to highlight later arrivals (Figure 2a). An f-k filter is used to suppress the dominant surface waves, followed by a reversal of the AGC. High-frequency noise is eliminated by the application of a bandpass filter with cut-off frequencies of 10 and 100 Hz. Three exemplary shot gathers of raw and processed data are displayed in Figures A1 and A2 (Appendix A). The data are then sorted into common midpoint (CMP) gathers. From this point, the further procedure, that is normal moveout (NMO) correction, stacking and migration, is performed following three different approaches. Approach 1 ("1D-v_{nmo}") follows a rather classical procedure. A velocity analysis using coherency-based velocity spectra (Neidell & Taner, 1971) is carried out for the central CMP (numbers 36–56). The obtained averaged 1D velocity function is used for NMO correction and stacking of the CMP gathers. For NMO correction and stacking approaches 2 and 3 use the final 2D FATT and FWI SH-velocity models, respectively, after each model is transferred from $v_{SH}(x,z)$ to $v_{SH}(x,t)$, the later equalling the interval velocity $v_{int}(x,t)$. Note that for all three approaches only traces within an offset of 3.0 m to the respective CMP are stacked because of the strong surface topography and expected dip of possible reflectors within the dike body. The usage of all traces would result in a smearing of the reflection point. After the data has been NMO-corrected and stacked, a migration to correct for imaging errors and to obtain a reflectivity image of the subsurface is applied. Thereby, dipping reflectors are relocated to their true subsurface position, amplitudes are shifted back to the reflector and diffractions collapse, leading to an improved spatial resolution. The resulting CMP section from approach 1 is migrated by Stolt migration (Stolt, 1978) and then converted to a depth section using the 1D stacking velocity. The CMP sections of approaches 2 and 3 are depth migrated applying a FD-migration algorithm using the FATT and FWI velocity models $v_{SH}(x,z)$, respectively. For migration, *sumigfd* from the Seismic Un*x package (Stockwell, 1999) is used with a maximum dip angle of the reflectors of 65°. The migration is followed by a bandpass filter with cut-off frequencies of 10 and 100 Hz. Subsequently, the migrated sections are smoothed by a semblance-based coherency filter (Milkereit et al., 1989). Finally, the traces of the migrated section are shifted to their respective positions below the topography.

4 | RESULTS

4.1 | Computational results

In Figure 3b, the final velocity model of the FATT is shown. Synthetic first arrival times are calculated in order to verify how well the final FATT velocity model can explain the field data. The RMS deviation is 2.7 ms for a total of 2256 calculated rays, the total absolute time difference amounts to 2.18 s and the total time difference is 0.28 s. The best fit between observed and calculated travel times is obtained for shot no. 39 ($x = 18.32$ m; Figure 3d) with a mean absolute time difference of 1.65 ms, whereas shot no. 15 ($x = 6.94$ m; Figure 3c) shows the worst fit with a mean absolute time difference of 4.9 ms. Larger deviations in travel time are observed for shot-receiver distances greater than 7 m on the inland side of the dike. The time differences between all shot-receiver pairs and the mean absolute time differences for each shot are shown in Figure C1, Appendix C.

The final FATT velocity model shows a velocity increase from approximately 60 m/s in the first 0.5 m below the surface to circa 160 to 180 m/s at $z = 2$–4 m. Velocity variations follow the topography of the dike. Shown here is only the velocity for the subsurface part that is covered by rays (cf. Figure C1c, Appendix C). A smoothed and downward extended version of this model serves as initial velocity model for the FWI.

The final velocity model of the FWI (Figure 4a) is obtained after 100 iterations through the 10 stages of the applied LBL strategy. The velocity ranges between 50 and 180 m/s. In general, the velocity

increases with depth and velocity variations follow the topography of the dike. The first meter is characterized by low velocities of 50 to 60 m/s. At the base of the dike on the inland side (**A**; $x \approx 16$ m), the velocity is slightly higher. The near surface low velocity layer has a thickness of approximately 1.5 m on the inland side of the dike (**B**). Low velocities to greater depths below the surface at the model's sides are visible (**C**). At depths of 0.5 to 3 m, the model has a velocity of about 150 m/s. Within the dike body, the velocity ranges between 80 and 120 m/s. A small zone of higher velocities becomes apparent on the land side between $x = 7$ m and $x = 13$ m and $z = -3$ m and $z = 0$ m (**D**). Below the dike body ($x = 3$ m to $x = 11$ m) a depression in the high velocity zone is visible (**E**).

A comparison between the resulting velocity models from FATT (Figure 3b) and FWI (Figure 4a) is only possible for the region covered by FATT. Here, the models show some similarities. In particular, the low velocities in the first meter below the surface and the high velocities for $z > 0$ m are evident in both models. In the FATT model, tomographic artefacts can also be seen as smearing of the high velocity along the raypaths for $x = 5$ to $x = 12$ m around $z = 0$ m. In the area of the dike body the models deviate from each other, whereby the FWI model shows clearly more structures and variability. In comparison, the FATT model is characterized by more or less homogenously increasing velocity.

The final density model (Figure 4b) yields values between 1700 and 2150 kg/m^3. Similar to the velocity model, the density variations follow the course of the topography of the dike. There are several similarities between the velocity and density models. Below an approximately 1-m-thick near-surface layer with a density of around 1800 to 1900 kg/m^3, a layer with higher density values (**F**, 1900–2100 kg/m^3) is apparent inside the dike. Below that, the density model values are again around 1800 kg/m^3. The lowest density values are found directly below the dike body between $x = 3$ m and $x = 10$ m and $z = 0$ m and $z \approx 3$ m (**G**). This area exhibits values of about 1700 kg/m^3 and correlates with the trench-shaped velocity layer (**E**) but is significantly deeper (≈2 m). The highest density with values greater than 2100 kg/m^3 (**H**) are found on the inland side of the dike between $x = 12$ m and $x = 20$ m for $z > 2$ m. Regarding the general density distribution, it may appear surprising that it does not increase monotonously with depth or due to the load of the dike and the resulting compaction of this layer. This may be caused by the composition of the fossil marsh and the early dikes which consisted mainly of clay with very high organic content, as this relatively loose material causes the reduced density values. Therefore, the density distribution inside the dyke has been inhomogeneous from the beginning.

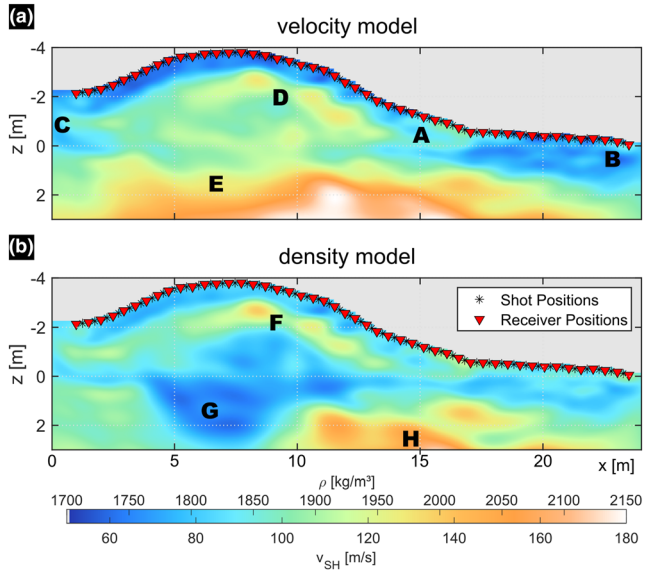

FIGURE 4 Results of the FWI of the acquired data set. The final velocity and density model are given in (a) and (b).

Figure 5 shows a comparison between the seismograms of the measured field data and the synthetic seismograms of the initial FWI model with a constant Q_{SH} of 5 (cf. Section 3.2.1) for shot gathers 23 ($x = 10.73$ m; top left) and 34 ($x = 15.81$ m; bottom left). The initial onsets show an overall good fit for all shot gathers. After the FWI, the waveforms of the synthetic data are in good agreement with the measured data in both the near and far offsets (Figure 5, right). The worst fit is obtained for shot no. 23 ($x = 10.73$ m; Figure 5, top right), the best fit is obtained for shot no. 34 (15.81 m; Figure 5, bottom right). Small deviations in the waveforms are still observed where the waveforms are characterized by overlapping arrivals, for example, close to $x = 0$ m. A zoom-in on the informative part of the waveform with all traces aligned according to the approximate first arrival time is shown in Figure B2 (Appendix B) to highlight the fit in onset, amplitude and phase of the data after the FWI.

All migrated sections (Figure 6a–c) show reflections (positive amplitudes are shaded) inside the dike body that follow the topography of the dike, in particular in the near subsurface. The main features are present in the sections of all three approaches. A comparison with the FWI velocity model (Figure 6c) shows a good agreement between strong reflections and changes in velocity. Within the dike body, two to three distinct reflectors are seen, for example a pronounced reflector is visible at the bottom of the approximately 1 to 1.5 m thick near-surface low velocity layer (**A** in Figure 6a). This reflector is clearly visible in all three sections. The high velocity layer, which forms a depression below the dike is highlighted with a white ellipse in Figure 6. The 1D-v_{nmo} approach tends to show a reflector mess, while in the other two approaches weak reflectors can be seen. Approach 2 shows a trough-shaped reflector on the sea-side of the dike (**B**), which does not correlate with the underlying FATT velocity model (Figure 6b). The same reflector is also seen in the section of approach 3, where it fits well with the FWI velocity model (Figure 6c, **C**). On the land side, no clear reflector is visible, but small negative amplitudes can be identified here (**D**). The deeper part of the depression (**E**) shows small (positive) amplitudes on some traces. This part of the depression is characterized by a visible reflector in the section of approach 1 (**F**).

Comparing the final sections (Figure 6; Figure D1, Appendix D), the differences as well as similarities are pointed out. Especially at both margins of the profile, individual separate reflections are more

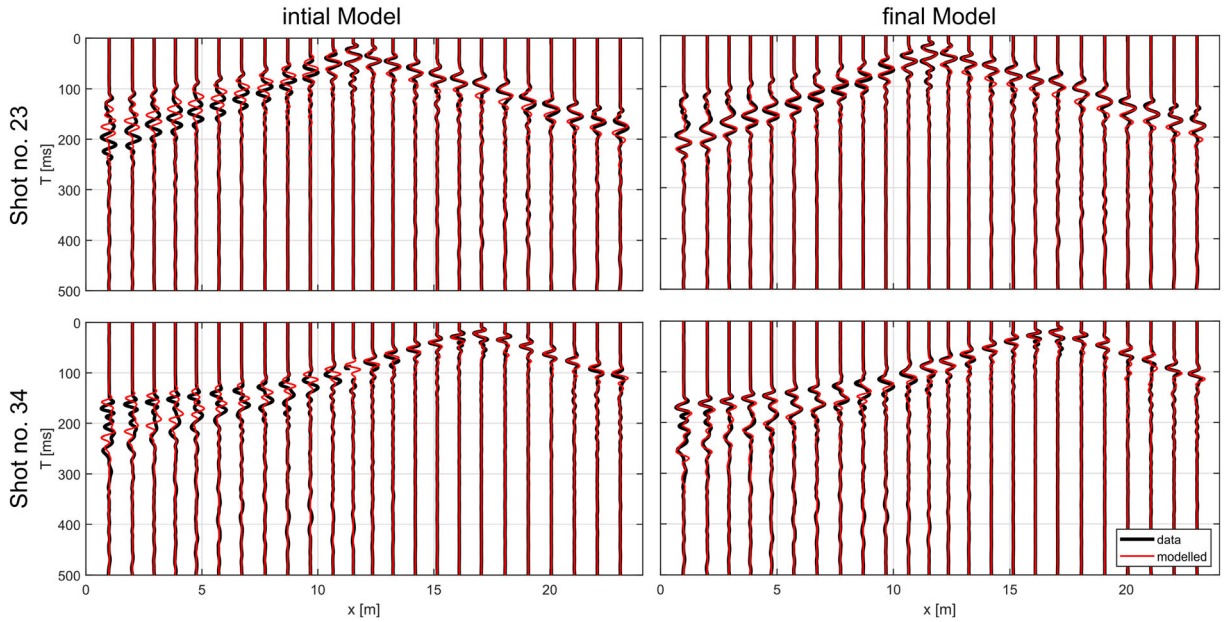

FIGURE 5 Comparison between measured (black) and modelled (red) data for the initial (left) and the final model (right) of the FWI. The top row shows the comparison for shot gather with the worst fit (no. 23; $x = 10.73$ m), the bottom row for the best fitted shot gather (no. 34; $x = 15.81$ m). The data are trace normalized and bandpass filtered (10–100 Hz). For reasons of clarity, only every second trace is shown.

clearly distinguishable in the sections processed following approach 2 and 3 compared with the section processed using approach 1. Otherwise, the section processed using approach 1 shows significantly more, but less continuous reflectors within the dike body and especially at the location of the trench observed in the velocity and density models (Figure 6a). This discontinuity and "mess" of reflectors may be caused by the application of the averaged and thereby simplified 1D velocity function during NMO correction, stacking and migration. The averaged 1D velocity function shows great variations with the travel time or respectively the depth, as well as standard deviations between 5 and 42 m/s (7%–35%). As the applied 1D model represents an average, lateral variations in the velocity distribution are not taken into account during processing. Thus, deviations from the "true" velocity model prevent a relocation of the reflections to their true subsurface position.

The question now arises why there is a depression visible in the FWI velocity model which is not obvious in the reflections? Looking at the final fit of the waveforms after the FWI, it can be seen that essentially the Love wave, as well as the direct and refracted wavefield are fitted well, whereas the reflections are only partially fitted. Especially deeper reflections ($t > 0.35$ s) are not taken into account by the FWI, as the amplitude-strong contributions of the surface wave predominate. However, surface waves are still sensitive to parameter changes in deeper parts of the subsurface. Furthermore, reflections do not only occur in the case of a change in velocity or density, but generally in the case of an impedance (product of shear velocity and bulk density) contrast. Here, the changes in both velocity and density, and thus in impedance are rather gradual than strong, which is attributable to minor changes within the sediment. If one now considers the impedance (Figure 6d) or its change (Figure 6e), the visible reflections coincide with impedance contrasts (**G**).

As the comparison between the approaches shows, there is a visible improvement in reflection seismic section when a 2D velocity model is used instead of the averaged 1D velocity function as in approach 1. This improvement is most evident in the upper 2 to 3 m, in which the reflectors obtained from approaches 2 and 3 are more continuous and consistent with the FWI models. This area is well covered by the Love wave, as well as by the direct and refracted wave and, as previous studies have shown, is of high resolution in the FWI model. The comparison with the impedance emphasizes the benefits of the inverted density model to explain all reflections. It should be noted that any artefact from the FWI velocity model will also be reflected in the final section, causing minor discrepancies. Therefore, one way to counteract this unwanted effect would be to use a version of the FWI velocity model smoothed by a 2D Gaussian filter instead. Comparing the resulting sections when using the original and a smoothed FWI velocity model (Figure D2, Appendix D), the largest differences are seen especially in the first 1.0–1.5 m below the surface. However, the maximum amplitude difference of about 0.01 is not large and is in the range of about 1% of the total maximum amplitude of 1. In the deeper range, the differences are even smaller.

4.2 | Interpretation and assessment of FWI results

The FWI is able to resolve individual sections within the dike, which is made evident by a comparison between the final models and an archaeological transect (Figure 7). In November 1974, a part of the

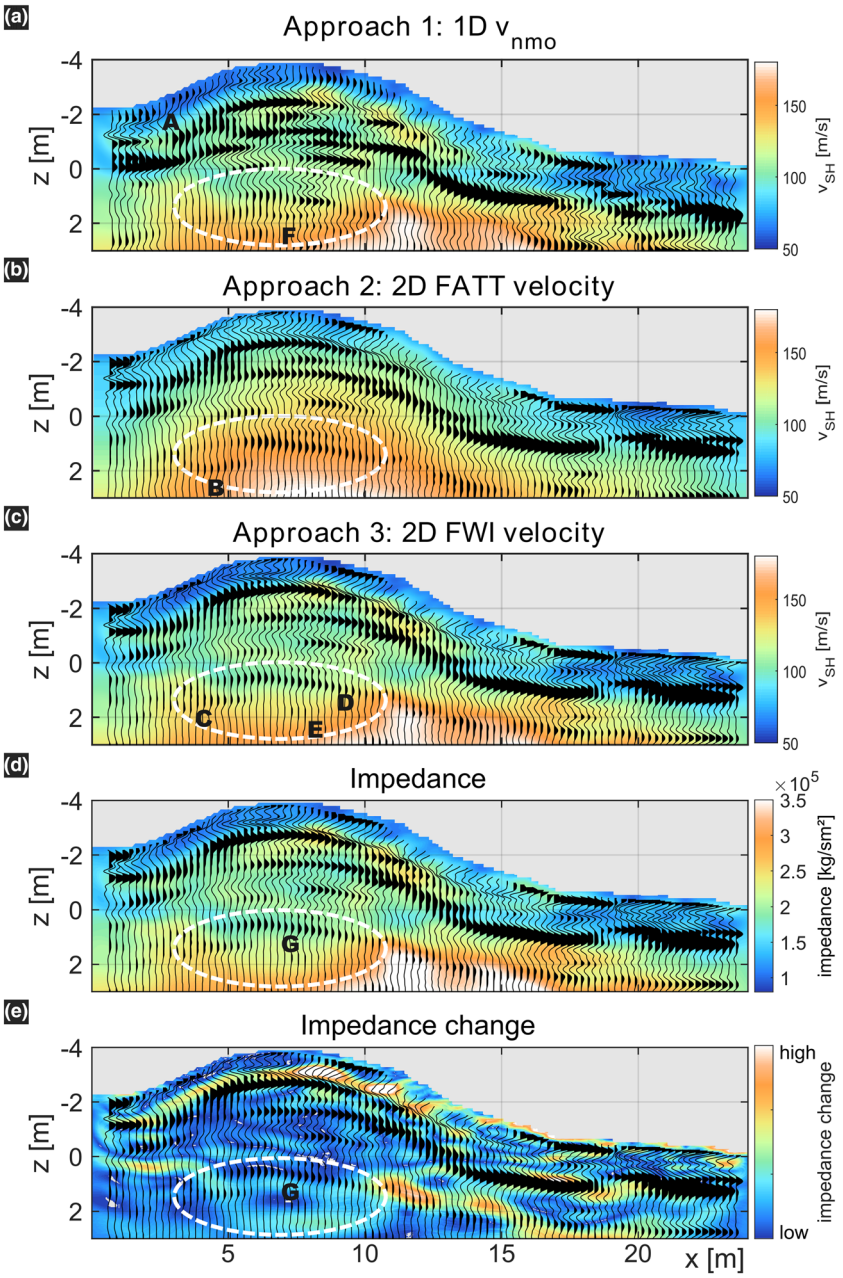

FIGURE 6 Comparison of the final migrated reflection seismic sections using three different approaches. The reflection seismic sections are shown as wiggle traces on top of the respective velocity model. The resulting section following approach 1 using an averaged 1D velocity model and Stolt migration is shown in (a); (b) and (c) show the resulting section following approaches 2 and 3, which use the 2D velocity models of the FATT (b) and FWI (c), respectively, subsequently followed by an FD migration. The impedance (d) and its change (e) show a better agreement with the reflection than the velocity model alone.

Schardeich about 150 m southwest of the acquired seismic profile was removed and its inner structure was described by Kühn (1989, 1992). Following the documentation of Kühn and Panten (1989), the construction phases of the dike seen in the excavated section between standard zero (NN, vertical datum used in Germany, "Normalnull") and NN + 4 m ($z = -4$ m) are shown in Figure 7a. For comparison, the elevations of the excavated section and the seismic profile have been combined. For $z > 0$ m, a soil of unstratified clay is present. Between 0 and −0.2 m, a layer of soil disturbed by the removal of the peat cover is observed. A zone (**I** in Figure 7a) consisting of alternating layers of sandy and clayey sediments is apparent between −0.2 and −0.5 m, with the sandy layers being a result of various storm surges. Layer **II** probably formed the first dike, which was further strengthened by another deposit (**III**) resulting in the second dike. The third dike (**IV**), with a crest height of up to 2.8 m, was strengthened inland by several distinct layers (**V**), consisting mainly of humic materials and peat inclusions. The final construction phase (**VI**) again raised the dike and widened it both on the seaside and inland. The second dike (**III**) is presumably the construction phase of the dike that surrounded the Großer Koog at the time of the devastating storm surge of 1362.

Although the removal of the dike and the excavation were carried out about 40 years ago and not at the same location as the seismic measurement, some similarities are recognizable in the comparison with the velocity (Figure 7b) and density models (Figure 7c). In particular, individual sections stand out due to the alternation of low and high velocities. Layer **I** with its higher seismic velocities above 100 m/s and low densities below 1850 kg/m^3 fits with the observed

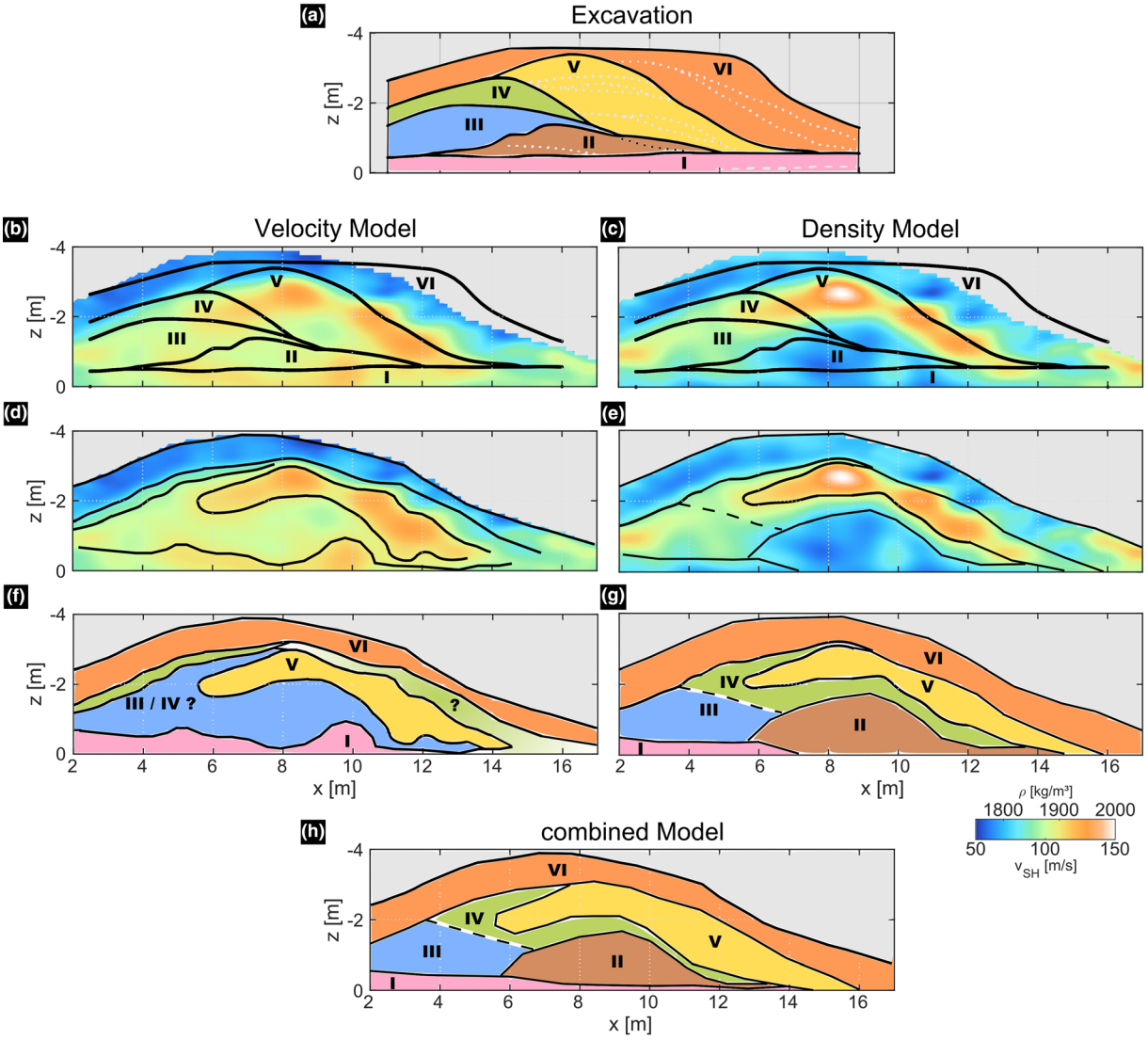

FIGURE 7 Comparison of the final FWI velocity (b,d) and density models (c,e) with the layers seen and described by Kühn (1992) in the archaeological transect. The layers documented by Kühn (1989) are shown in (a) and overlaid on the final velocity and density models in (b) and (c), respectively. Based on isolines of several velocities (d) and densities (e), models of the internal structure are estimated (f,g). In (h), a combined model of the internal structure is shown. For the used isolines of (d) and (e), see Figure E1 and Table E1 in Appendix E.

alternating layers of sand and marine clay as described by Kühn (1989). Layers **II**, **III** and **IV** are characterized by velocities between 80 and 100 m/s and are not distinguishable in the seismic velocities as they probably consist of the same material (Figure 7d–g). Especially Layer **II** is recognizable in the density model with densities of less than 1800 kg/m^3. Similar to the velocity model, Layers **III** and **IV** cannot be clearly distinguished. Layer **V** is clearly identified through increased velocities as well as densities. Humic materials and peat are characterized by a rather low seismic velocity (40–80 m/s; Corradini et al., 2020), what contradicts the association of the high velocity zone with Layer **V**. As Kühn (1989) described this layer to be consisting of peat inclusions, their impact on the overall seismic velocity is either rather small or the high velocity represents the surface of that dike, which has been compressed over the years resulting in higher velocities. The top layer (**VI**) is also easily recognizable by the low densities and velocities in the first 1.0 m below the surface. This fits well with the observations of Köhn et al. (2018) as they also found a layer of low seismic velocities in the top 1.5 m below the surface. Note that today, the area around the dike as well as the dike remnant is used as cattle pasture, which may have caused parts of it to be eroded or compacted.

From the individual interpretations of the velocity (Figure 7f) and density (Figure 7g) models, a combined interpretational model was deduced (Figure 7h) by superposition of both models, taking their similarities and individualities into account and also considering the seismic impedance. It clearly shows that all layers of the dike as seen in the excavation can be identified and partially assigned to the alternating low and high velocity and density layers, respectively.

4.3 | The dike's imprint: FWI result

Both the velocity model and the density model show a depression-like structure (Figures 4 and 6). This structure is located directly below the highest point of the dike between $z = 0$ m and $z = 1$–2 m, respectively, and is also seen in the change of seismic impedance. The contour line of an impedance change of 1200 kg/(sm^2), result in depressions of approximately 0.8–1.0 m (Figure 8a). A pronounced reflection of positive amplitude can also be seen following this contour line (Figure 6e). This layer boundary runs roughly horizontal at shallower depths on the seaward side (approximately $z = 0.25$ m) and greater depths on the landward side (approximately $z = 0.5$ m) and presumably represents the historical land surface. These observations fit well with Kühn (1989), who found undisturbed soil in $z \geq 0$ m in the excavation, and Josy (2020), who identified the former land surface at a depth of about 0.4 m below a layer of storm surge sediments in a coring in an area where the dike was removed.

The subsidence caused by the load of the dike is analysed using a geotechnical calculation. The subsidence or consolidation S is given by the following relation (Rechtern, 2003):

$$S = \frac{\sigma \cdot z}{E_s} = \frac{\gamma \cdot h \cdot z}{E_s} = \frac{g \cdot \rho \cdot h \cdot z}{E_s}, \quad (2)$$

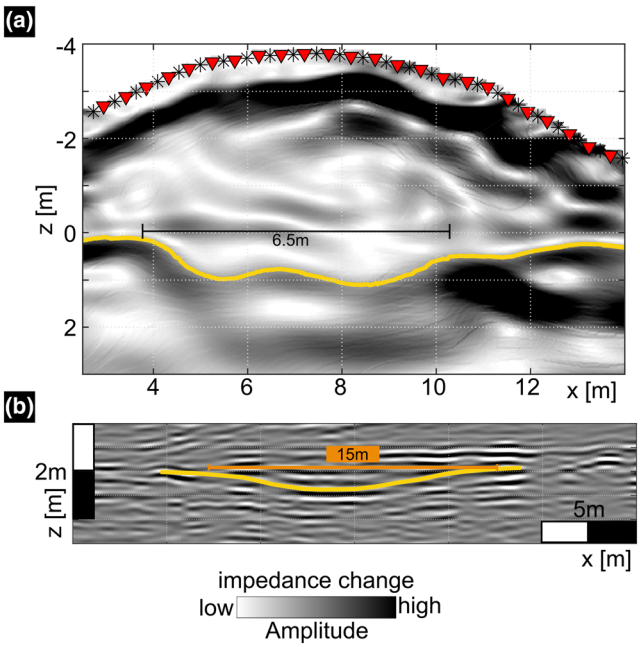

FIGURE 8 Observed depression in the FWI change of impedance model (a) based on the contour of an impedance change of 1200 kg/sm^2, marked in yellow. In comparison, a seismic reflection profile from the Wadden Sea (similar to fig. 6b in Wilken et al., 2022 and fig. 12 in Schwardt et al., 2021) is shown in (b) with the depression marked in yellow. The depth scales are the same for both profiles. Note the difference on the horizontal scales.

with the stiffness modulus E_s, the thickness z of the layer on which the load is applied and the normal stress σ. The normal stress σ can be determined from the height h of the load, that is, the raised dike, and the specific weight γ of the used material.

The layer where the dikes imprint is most likely to be seen is the historical land surface which consists of clay. Considering the findings of the excavation as well as of a coring in the area where the dike has been removed (Josy, 2020), the historical land surface is found in a depth of about 4 to 4.5 m below dike crown ($z = 0$ to $z = 0.5$ m in Figure 8a). The layer has a thickness of 3 m, with marine shallow water sediments below according to the coring (Josy, 2020). In the excavation, only the topmost 0.2 m of the clay layer were evident on the land side (Kühn, 1989). By taking the average density $\rho = 1850$ kg/m^3 from the FWI model, a gravitational acceleration of $g = 9.81$ m/s^2, a height of the dike of $h = 4.5$ m, a thickness of the deformed clay layer of 3.0 m, and a stiffness modulus of $E_s = 0.5 \cdot 10^6$ kg/(s^{2}m) (Kuntsche, 2016), a subsidence of approximately $S = 0.5$ m is obtained. This corresponds approximately to the setting below the dike as observed in the impedance change model (Figure 8a), the seismic velocity model for the velocity contour of 115 m/s (Figure 4a) and the amount of subsidence for the historical dikes seen in the marine seismic reflection profiles (Figure 8b) in Wilken et al. (2022) mentioned in the introduction. Note that the calculated specific weight ($\approx 18.15 \cdot 10^3$ kg/(s^{2}m^2)) of the dike fits well with typical values for the expected clay ($15.5 \cdot 10^3$ kg/(s^{2}m^2)) and sand ($18.5 \cdot 10^3$ kg/(s^{2}m^2)), whereas the specific weight for peat is a little lower ($11 \cdot 10^3$ to $13 \cdot 10^3$ kg/(s^{2}m^2); Kuntsche, 2016).

Since the calculated subsidence corresponds approximately to the seismically observed value, the question now arises if, as a reverse conclusion, the height of the eroded dike in the tidal flats can be inferred from the observed subsidence (Figure 8b). The dike has been of the same age and largely destroyed during the storm surge of 1362 (e.g., Wilken et al., 2022). From historical sources, corings and marine seismic data, the amount of deformation is estimated to $S = 0.2$ to $S = 0.4$ m (Busch, 1960; Wilken et al., 2022). Assuming that the former dike has been constructed of similar material as observed here because of the same age and environment, we apply the same mean density value and stiffness modules. The deformed layer represents the former land surface before the dike construction. That layer is assumed to have had a thickness of about 2.5–3 m. Thus, a depression of 0.2 m results in a height of 2.2 m and a depression of 0.4 m in a height of 4.4 m. This corresponds to the assumptions of Bantelmann and Fischer (1967), Meier (2007, 2016) and Muuß (1927). Meier (2007, 2016) specifies the crown height of the Niedam dike to be at least NN + 2 m, while Bantelmann and Fischer (1967) and Muuß (1927) assume a dike height of about NN + 3.5 m to NN + 4.0 m. A comparable height of the dikes for the time around 1362 is also given by Niemeyer et al. (1996). Differences in depth and width of the footprint between the Schardeich and the tidal flats are attributed to the width of the dike base and the function of the dikes. While the Schardeich served as middle dike, the eroded dike represented a sea dike, which required a wider dike base. As there is a lot of organic material contained, there may have occurred some uplift after the dike has

been eroded by the North Sea. This may possibly have been intercepted by newly deposited tidal flat sediments as well as by the water masses.

4.4 | The internal structure and the dike's imprint from a reflections seismics point of view

When looking at the reflections of the individual construction phases of the dike, it is important to consider the vertical resolution. It depends on both velocity and depth and decreases with depth due to absorption effects. The top and bottom of a layer are optically separable in the seismogram as two individual reflectors if the layer thickness is greater than one quarter to one eighth of the mean wavelength λ_m. Table F1 (Appendix F) lists the resolutions for the mean velocities at the respective depth below the surface for a frequency of 30 Hz (dominant frequency). The vertical resolution varies between 0.3 and 0.6 m at 1 m below the surface and between 0.6 to 1.1 m at 10 m below the surface. The thickest areas of each layer are well above the vertical resolution, so they should be visible as individual reflections in the final seismic section.

Reflections occur when there is a change in seismic impedance. The change in impedance (Figures 6e and 8a) is not large enough at the location of the depression in the velocity and density models and therefore, no pronounced reflection occurs. In fact, only small changes in seismic impedance in the region of the depression are observed, whereby strong reflections coincide with larger impedance changes (Figure 6e). By calculating the impedance and its change, a comparison with the marine data is thus possible. These show P-wave data and reflections generated by impedance contrasts, which, in the marine near-surface environment, are mainly caused by density variations. The depression is clearly visible in the marine seismic data by Wilken et al. (2022). However, due to the 100-fold higher frequencies (4 kHz vs. 30 Hz) and the approximately 10-fold higher velocities (approximately 1500 m/s vs. approximately 150 m/s), the marine seismic data offers a significantly higher vertical resolution of about 0.05 to 0.1 m. In terms of horizontal resolution, the first Fresnel zone has to be considered, which is also depth dependent. Looking at the spatial sampling, the reflection profile on land with an average trace spacing of 0.2 to 0.25 m has a slightly lower data coverage compared with the marine data with an average trace spacing of 0.16 m (Wilken et al., 2022).

5 | DISCUSSION

In the present paper, we applied a 2D full waveform inversion to a seismic SH-wave profile in order to prospect the interior structure of a historical dike. The main objective was to investigate whether the FWI is capable of imaging the individual construction phases of the dike and whether a dike imprint similar to the one observed in the tidal flats (Muuß, 1927; Wilken et al., 2022) is visible in the seismic data. To classify the results with respect to the internal structure, we also consider an archaeological transect through the dike, allowing the possibility of ground truthing. The results are thus placed in their archaeological context, compared with other historical dikes and the obtained information about the dikes imprint are evaluated in terms of their validity in a geotechnical sense. Further, we discuss the results with regard to the resolution capabilities of both the FWI and the reflection seismics, and in addition, a comment is made in comparison to other methods.

5.1 | Comparison of seismic methods in relation to other geophysical methods applied on dikes and the potential of the FWI to resolve the internal dike structure

While potential field methods such as ERT are used for the investigation of mainly modern dikes, seismic methods play a minor role (e.g., Fauchard & Mériaux, 2007; Niederleithinger et al., 2012). Seismic methods that have been used are active and passive multichannel analysis of surface waves (MASW; e.g., Joubert et al., 2018; Le Feuvre et al., 2015; Pageot et al., 2020), while reflection and refraction seismic methods are rarely applied (e.g., Bièvre & Norgeot, 2005; Jaksch, 2009). This is mainly due to the fact that investigations on modern dikes are supposed to reveal weak points such as water infiltration, water pathways, cavities and damage caused by animals, which requires a very high spatial resolution (e.g., Rittgers et al., 2015). MASW is not able to resolve such small spatial changes below 1–2 m (e.g., Karl et al., 2011) and although reflection and refraction seismic methods provide a good penetration depth, their resolution is also below the requirements. In terms of both resolution and data acquisition time, GPR would be a good choice, but the penetration depth is also very limited, especially concerning the height of modern dikes (>8 m at the German North Sea coast; Hofstede, 2019).

The FWI is able to provide a detailed velocity and density model of the subsurface as has been shown by several previous studies (e.g., Köhn et al., 2019; Mecking et al., 2021; Schwardt et al., 2020). Based on the comparison of the waveforms between the measured field data and the synthetic data (Figure 5), it can be seen that the model is able to fit the data correctly. Both the initial onsets of the refracted waves and the Love wave field are successfully fitted. Clearly, the velocity model shows zones of low velocity near the surface on both margins of the model, which presumably results from the adjustment to the side reflections and coincide with the road and water trench adjacent to the dike.

One issue that has remained unresolved for FWI is the accurate determination of the structural resolution capability in concrete field cases. In terms of wave theory, the maximum achievable resolution corresponds to the quarter-wavelength criterion well known from classical reflection seismics. However, previous studies have shown the high-resolution capabilities of the applied FWI algorithm (e.g., Dokter et al., 2017; Köhn et al., 2019; Rusch et al., 2022). All studies show that structures with dimensions smaller than 1.0 m by 1.0 m could be reliably resolved, making the FWI a promising tool for the investigation of dikes. Especially Schwardt et al. (2020) showed

that the FWI is able to obtain a very good spatial resolution in the near-surface area down to 2 m depth, and in Köhn et al. (2019) sediment changes in the order of 0.2 to 0.5 m could be resolved by the FWI algorithm. Using synthetic resolution tests, Dokter et al. (2017) investigated the spatial resolution for the same FWI algorithm. Rusch et al., 2022 applied the FWI as part of a multimethod geophysical study to distinguish between interpretation hypothesizes for observed structures obtained by nonseismic methods achieving a resolution on the decimetre scale and Mecking et al. (2021) use FWI for cavity detection inside a high monumental antique grave mount. The potential of the FWI to resolve the internal structures of a sea dike was investigated in a study by Köhn et al. (2018), where a high correlation between the SH-wave velocity structure and the lithology known from corings was observed. They found a relationship between marine clay and areas of low seismic velocity as well as sand layers and high seismic velocities. Moreover, similar to this study, the surface layer (about 1.5 m) shows low seismic velocities, and the overall structure is characterized by alternating layers of higher and lower velocity. The study by Köhn et al. (2018) shows higher velocities on the land side compared with the seaside, this behaviour is also observed here. Hence, there are some similarities in the investigation of historical and modern dikes by means of seismic waveform inversion, highlighting the resolution capabilities of the FWI with regard to lithological changes.

Furthermore, the FWI offers the possibility of FD migration or reverse time migration of the reflection seismic data, which leads to an improvement of the final section and a better agreement of the reflections with the velocity model. Thereby, 2D velocity differences and especially topographic effects are considered and allow a combined interpretation of the data. In addition, it should be emphasized that only the joint inversion of velocity and density enables the determination of the seismic impedance and its change, which ultimately allows a comprehensive interpretation and explanation of the reflections and their deviations from the velocity model.

5.2 | Comparison of the model values with an archaeological transect

The obtained velocity and density values between 60 and 150 m/s and 1700 and 2100 kg/m^3 are in good agreement with literature values of various studies (e.g., Schön, 1983; cf. Table 1). Likewise, the quality factor of $Q_{SH} = 5$ also falls within the expected range. For sands, Q_{SH} values between 5 and 30 have been observed so far, depending on water saturation and pressure (e.g., Cox, 1999; Kudo & Shima, 1970: $5 \leq Q_{SH} \geq 20$; Podolski, 2015: $Q_{SH} = 6, 13$). The FWI thus delivers values that meet expectations.

5.3 | Classification of the results in relation to other historical dikes

There are many dikes of the same age that have been described as part of excavations or transects. Comparable to today's dikes, the dike heights have evolved depending on the respective local mean high tide and are considered in relation to normal zero. For the first dikes from the 11th and 12th centuries, heights of about NN + 1.6 m are assumed. These dikes were raised to NN + 2 m in the 13th and first half of the 14th century until the storm surge of 1362. The dikes that remained after the flood were raised again by 0.8 m, likewise it is assumed that there were further increases until the 17th century to NN + 4 m (e.g., Meier, 2016; Newig & Petersen, 1995). Based on the reconstructions by Busch (1963), Meier (2016) assumes that the dike crests at that time were about 2.44 m above the mean high tide. There are other examples of historical dikes that already existed at the time of the storm surge of 1362. The dike surrounding the Alter Koog on Nordstrand had a crown height of NN + 2 m in the 13th and 14th centuries (Kühn, 1989; Meier, 2011), with the dike base only a few decimetres above NN (Newig & Petersen, 1995). Busch (1963) specifies the crest height of another section of the same dike to have

TABLE 1 Literature values for velocities and densities for the presumed materials of the dike with their corresponding references in comparison with the values obtained in this study.

Material	Shear wave velocity (m/s) 60–150	Density (kg/m^3) 1700–2100	Reference This study
Sand		2100	Arnott et al. (2005)
	30–450	1800–2050	Schön (1983, 2015)
Silt		1850–2100	Schön (1983)
Clay	180–2100	1450–1900	Schön (1983, 2015)
Sand – Silt – Clay		1740	Arnott et al. (2005)
Loam	90–360		Schön (1983, 2015
Peat	40–80	80–300	Corradini et al. (2020)
Modern dike	60–140		Köhn et al. (2018)
Marine near surface sediments (North Sea)	85–195		Hamilton (1977)
	50–140		Richardson (2002)
	95–160	1700	Podolski (2015)
0–8 m depth in tidal flats (Netherlands)	100–172		Gabriels et al. (1987)

been about 2.5 m above mean high tide and at about NN + 2 m in the 14th century. An approximately 1.0 m high clay dike on the island of Sylt (Morsum-Odde) is considerably smaller, but due to the high position of the dike base it was located at NN + 2.6 to NN + 2.8 m. This dike has a similar base width of about 6.5 m as the Schardeich is assumed to have had in the 12th century (Busch, 1939). Other examples are the Stollhammer Ahndeich (Butjadingen, Wesermarsch, Lower Saxony) with a height of almost 2 m compared with the surrounding areas (Ey, 2010) or the summer dike around the St. Johannes Koog, Eiderstedt, with an assumed height of NN + 1.5 m in the 12th century (Meier, 2004). In the comparison with the observations of other historical dikes of similar age, the back-calculation from the imprint yields comparable height values for the dike remains in the tidal flats.

6 | CONCLUSIONS

We applied a combination of FWI and reflection seismics to investigate the historical Schardeich on the island of Pellworm in the German North Sea. The questions posed at the beginning can now be answered: (1) From a methodological point of view, the present results show, especially in comparison with the excavation, that the FWI is able to depict the internal structure, that is, individual construction phases of the dike. Furthermore, there is a good agreement between the impedance model derived from the inverted velocity and density models and the reflection seismic section. Especially the youngest layer (layer **VI**; top 1.0 to 1.5 m), as well as parts of layer **V** and the former land surface (**I**) can be derived well from the velocity model. (2) In the impedance contrast model, the investigated dike also shows an imprint of about 0.75 m, which is, however, of slightly greater depth than the reflector observed in the tidal flats in the Rungholt area. (3) The observed depression lies within the range of the calculated subsidence of approximately 0.5 m. From this, a height between 2.2 to 4.4 m for the dike mapped in the tidal flat could be derived.

In summary, the FWI provides a high-resolution velocity model that allows conclusions to be drawn about the internal dike structure as well as the deeper subsurface. In combination with the density model, further statements on lithology and compaction are possible. The FWI not only provides a detailed velocity and density model, but also contributes to the improvement of reflection seismics and thus to joined interpretation possibilities through these reliable and high-resolution 2D models, especially in the near-surface area. The comparison between the approaches illustrates the resolution problems of reflection seismics and the benefits of FWI. The joint inversion of velocity and density enables the determination of the seismic impedance, which ultimately allows a comprehensive interpretation and explanation of all reflections. This makes the FWI a promising tool not only for the investigation of historical dikes, but also for the investigation of modern dikes by allowing the detection of small-scale zones of weakness and damages.

ACKNOWLEDGEMENTS

The work presented here was funded by the German Research Foundation (DFG) in projects (RA 496/26-2) situated in the frame of the Priority Program 1630 "Harbours from the Roman Period to the Middle Ages" (Von Carnap-Bornheim & Kalmring, 2011). The FWI inversions were performed on the NEC-HPC Linux-Cluster at the computation centre of Kiel University. Working permits were kindly issued by the Schleswig-Holstein State Office for Coastal Protection, National Park and Marine Protection (Landesbetrieb für Küstenschutz, Nationalpark und Meeresschutz, Schleswig-Holstein) and the Schleswig-Holstein Archaeological State Office (Archäologisches Landesamt Schleswig-Holstein). We like to thank J. Ohnasch for permission to conduct the measurements on his property and P. Leineweber for his support during fieldwork. Open Access funding enabled and organized by Projekt DEAL.

CONFLICT OF INTEREST STATEMENT

The authors declare that they have no known competing financial interests or personal relationships that could have appeared to influence the work reported in this paper.

DATA AVAILABILITY STATEMENT

The data that support the findings of this study are available from the corresponding author upon reasonable request.

ORCID

Michaela Schwardt https://orcid.org/0000-0002-5639-3945

REFERENCES

Arnott, S. H., Dix, J. K., Best, A. I., & Gregory, D. J. (2005). Imaging of buried archaeological materials: The reflection properties of archaeological wood. *Marine Geophysical Researches*, *26*(2-4), 135–144. https://doi.org/10.1007/s11001-005-3713-x

Bantelmann, A., & Fischer, F. (1967). Die Landschaftsentwicklung an der schleswig-holsteinischen Westküste, dargestellt am Beispiel Nordfriesland. Eine Funktionschronik durch fünf Jahrtausende. *Die Küste*, *14*(2), 5–99.

Bauer, E., Fischer, L., Joachim, H., Kühn, M. M., & Meier, D. (2001). 4.3 The Schleswig-Holstein Wadden Sea Region.

Bièvre, G., & Norgeot, C. (2005). On the use of geophysical methods for the characterization of earth dams: A case study on the Canal du Centre. Bulletin des Laboratoires des ponts et chaussée, 85–107.

Bohlen, T. (2002). Parallel 3-D viscoelastic finite difference seismic modelling. *Computers & Geosciences*, *28*(8), 887–899. https://doi.org/10.1016/S0098-3004(02)00006-7

Busch, A. (1936). Neue Beobachtungen im Rungholt-Watt im Jahre 1935. Die Heimat, Heft 3.

Busch, A. (1939). Alte Deichquerschnitte auf Sylt, ein Beitrag zu den Fragen der Anfangsentwicklung des Deichbaues. Westküste *2*, *1*, (2, 1), 116–122.

Busch, A. (1960). Eine alte Landoberfläche und Kulturspuren im Nordstrander Watt. *Die Küste*, *08*(8), 124–130.

Busch, A. (1963). Alte und neue Deichprofile von Strucklahnungshörn (Nordstrand) und der Anstieg des Meeresspiegels. *Die Heimat*, *70*(H. 6), 4–11.

Choi, Y., & Alkhalifah, T. (2012). Application of multi-source waveform inversion to marine streamer data using the global correlation norm.

Geophysical Prospecting, *60*, 748–758. https://doi.org/10.1111/j.1365-2478.2012.01079.x

Corradini, E., Dreibrodt, S., Erkul, E., Groß, D., Lübke, H., Panning, D., Pickartz, N., Thorwart, M., Vött, A., Willershäuser, T., Wilken, D., Wunderlich, T., Zanon, M., & Rabbel, W. (2020). Understanding wetlands stratigraphy: Geophysics and soil parameters for investigating ancient basin development at Lake Duvensee. *Geosciences*, *10*(8), 314. https://doi.org/10.3390/geosciences10080314

Cox, M. (1999). *Static corrections for seismic reflection surveys*. Society of Exploration Geophysicists. https://doi.org/10.1190/1.9781560801818

Dines, K. A., & Lytle, R. J. (1979). Computerized geophysical tomography. *Proceedings of the IEEE*, *67*(7), 1065–1073. https://doi.org/10.1109/PROC.1979.11390

Dokter, E., Köhn, D., Wilken, D., De Nil, D., & Rabbel, W. (2017). Full waveform inversion of SH-and Love-wave data in near-surface prospecting. *Geophysical Prospecting*, *65*(S1), 216–236. https://doi.org/10.1111/1365-2478.12549

Ey, J. (2010). Initiation of dike-construction in the German clay district. *Wadden Sea Ecosystem*, *26*, 179–183.

Fauchard, C., & Mériaux, P. (2007). Geophysical and geotechnical methods for diagnosing flood protection dikes 124 éditions Quae.

Forbriger, T., Groos, L., & Schäfer, M. (2014). Line-source simulation for shallow-seismic data. Part 1: Theoretical background. *Geophysical Journal International*, *198*(3), 1387–1404. https://doi.org/10.1093/gji/ggu199

Gabriels, P., Snieder, R., & Nolet, G. (1987). In situ measurements of shear-wave velocity in sediments with higher-mode Rayleigh waves. *Geophysical Prospecting*, *35*(2), 187–196. https://doi.org/10.1111/j.1365-2478.1987.tb00812.x

Groos, L. (2013). 2D full waveform inversion of shallow seismicRayleigh waves. PhD thesis, Karlsruhe Institute of Technology, Germany.

Groos, L., Schäfer, M., Forbriger, T., & Bohlen, T. (2014). The role of attenuation in 2D full-waveform inversion of shallow-seismic body and Rayleigh waves. *Geophysics*, *79*(6), R247–R261. https://doi.org/10.1190/geo2013-0462.1

Hadler, H., Vött, A., Newig, J., Emde, K., Finkler, C., Fischer, P., & Willershäuser, T. (2018). Geoarchaeological evidence of marshland destruction in the area of Rungholt, present-day Wadden Sea around Hallig Südfall (north Frisia, Germany), by the Grote Mandrenke in 1362 AD. *Quaternary International*, *473*, 37–54. https://doi.org/10.1016/j.quaint.2017.09.013

Hadler, H., Wilken, D., Wunderlich, T., Fediuk, A., Fischer, P., Schwardt, M., Willershäuser, T., Rabbel, W., & Vött, A. (2018). 16 Drowned by the Grote Mandrenke in 1362. In *Waddenland Outstanding* (pp. 239–252). Amsterdam University Press. https://doi.org/10.1515/9789048537884-017

Hamilton, E. L. (1977). Shear-wave velocity versus depth in marine sediments: A review. *The Log Analyst*, *18*(01), SPWLA-1977-vXVIIIn1a5.

Hoffmann, D. (2004). Holocene landscape development in the marshes of the west coast of Schleswig-Holstein, Germany. *Quaternary International*, *112*(1), 29–36. https://doi.org/10.1016/S1040-6182(03)00063-6

Hofstede, J. (2019). Küstenschutz in Schleswig-Holstein: ein Überblick über Strategien und Maßnahmen. *Die Küste*, *87*(87), 287–302.

Jaksch, K. (2009). Seismisches Monitoring an lehmigen Modelldeichen. Ph.D. thesis, TU Bergakademie Freiberg. Available at http://nbn-resolving.de/urn:nbn:de:bsz:105-7556238

Josy, K. (2020). Landschaftsentwicklung und Deichbau in Nordfriesland. Geoarchäologische Untersuchungen am Schardeich auf Pellworm. Bachelor-Thesis. Mainz University.

Joubert, A., Le Feuvre, M., & Côte, P. (2018). Passive monitoring of a sea dike during a tidal cycle using sea waves as a seismic noise source. *Geophysical Journal International*, *214*(2), 1364–1378. https://doi.org/10.1093/gji/ggy180

Karl, L., Fechner, T., Schevenels, M., François, S., & Degrande, G. (2011). Geotechnical characterization of a river dyke by surface waves. *Near Surface Geophysics*, *9*(6), 515–527. https://doi.org/10.3997/1873-0604.2011030

Köhn, D., De Nil, D., Kurzmann, A., Groos, L., Schäfer, M., & Heider, S. (2014). DENISE User Manual. *Christian-Albrechts-Universität (Kiel) und Karlsruher Institut für Technologie (Karlsruhe)*. available at https://danielkoehnsite.files.wordpress.com/2021/06/manual_denise.pdf

Köhn, D., De Nil, D., Kurzmann, A., Przebindowska, A., & Bohlen, T. (2012). On the influence of model parametrization in elastic full waveform tomography. *Geophysical Journal International*, *191*(1), 325–345. https://doi.org/10.1111/j.1365-246X.2012.05633.x

Köhn, D., Wilken, D., De Nil, D., Wunderlich, T., Rabbel, W., Werther, L., Schmidt, J., Zielhofer, C., & Linzen, S. (2019). Comparison of time-domain SH waveform inversion strategies based on sequential low and bandpass filtered data for improved resolution in near-surface prospecting. *Journal of Applied Geophysics*, *160*, 69–83. https://doi.org/10.1016/j.jappgeo.2018.11.001

Köhn, D., Wilken, D., Meier, T., Steinkraus, T., Schulte-Kortnack, D., De Nil, D., Kirsch, R., & Rabbel, W. (2018). Sea dike evaluation by SH full waveform inversion. In *24th European Meeting of Environmental and Engineering Geophysics: Near Surface Geoscience Conference & Exhibition 2018*. European Association of Geoscientists and Engineers.

Komatitsch, D., & Martin, R. (2007). An unsplit convolutional perfectly matched layer improved at grazing incidence for the seismic wave equation. *Geophysics*, *72*(5), SM155–SM167. https://doi.org/10.1190/1.2757586

Kudo, K., & Shima, E. (1970). Attenuation of shear wave in soil: Bulletin of the Earthquake Research Institute. 48, 145–158.

Kühn, H. J. (1989). Deiche des frühen Mittelalters und der frühen Neuzeit. Der frühe Deichbau in Nordfriesland. Archäologisch-historische Untersuchungen, Bredstedt, 11–62.

Kühn, H. J. (1992). *Die Anfänge des Deichbaus in Schleswig-Holstein* (Vol. 42). Westholsteinische Verlagsanstalt Boyens.

Kühn, H. J., & Panten, A. (1989). Der frühe Deichbau in Nordfriesland. Archäologisch-historische Untersuchungen. Nordfriisk Inst, 94.

Kuntsche, K. (2016). *Geotechnik: erkunden-untersuchen-berechnen-ausführen-messen*. Springer-Verlag. https://doi.org/10.1007/978-3-8348-2020-4

Le Feuvre, M., Joubert, A., Leparoux, D., & Cote, P. (2015). Passive multichannel analysis of surface waves with cross-correlations and beamforming. Application to a sea dike. *Journal of Applied Geophysics*, *114*, 36–51. https://doi.org/10.1016/j.jappgeo.2014.12.014

Levander, A. R. (1988). Fourth-order finite-difference P-SV seismograms. *Geophysics*, *53*(11), 1425–1436. https://doi.org/10.1190/1.1442422

Mecking, R., Köhn, D., Meinecke, M., & Rabbel, W. (2021). Cavity detection by SH-wave full-waveform inversion—A reflection-focused approach. *Geophysics*, *86*(3), WA123–WA137. https://doi.org/10.1190/geo2020-0349.1

Meier, D. (2004). Man and environment in the marsh area of Schleswig–Holstein from Roman until late Medieval times. *Quaternary International*, *112*(1), 55–69. https://doi.org/10.1016/S1040-6182(03)00065-X

Meier, D. (2007). *Schleswig-Holsteins Küsten im Wandel: von der Eiszeit zur globalen Klimaerwärmung*. Boyens.

Meier, D. (2008). The historical geography of the German North-Sea coast: A changing landscape. *Die Küste*, *74*, 18–30.

Meier, D. (2011). *Schleswig-Holstein im frühen Mittelalter: Landschaft-Archäologie-Geschichte*. Boyens.

Meier, D. (2016). Landesausbau, Umweltwandel und Sturmfluten im hohen und späten Mittelalter in den südlichen nordfriesischen Uthlanden. In M. Mersch (Ed.), *Mensch-Natur-Wechselwirkungen in der Vormoderne* (Vol. 109). Universitätsverlag Göttingen.

Milkereit, B., Spencer, C., Agterberg, F. P., & Bonham-Carter, G. F. (1989). Noise suppression and coherency enhancement of seismic data. In

Statistical application in the earth sciences (Vol. 89) (pp. 243–248). Geological Survey of Canada.

Müller-Wille, M., Higelke, B., Hoffmann, D., Menke, B., Brande, A., Bokelmann, K., Saggau, H. & Kühn, H. (1988). Norderhever-Projekt - Landschaftsentwicklung und Siedlungsgeschichte im Einzugsgebiet der Norderhever (Nordfriesland). Neumünster.

Muuß, R. (1927). *Rungholt*. Friesen Verlag.

Neidell, N. S., & Taner, M. T. (1971). Semblance and other coherency measures for multichannel data. *Geophysics*, *36*(3), 482–497. https://doi.org/10.1190/1.1440186

Newig, J. (2004). Die Küstengestalt Nordfrieslands im Mittelalter nach historischen Quellen. *Coastline Reports*, *1*, 23–36.

Newig, J., & Petersen, M. (1995). Eine Klassifizierung von Deichen an der Nordseeküste–erläutert an Beispielen aus Schleswig-Holstein. *Schriften des Naturwissenschaftlichen Vereins für Schleswig-Holstein*, *65*, 67–106.

Niederleithinger, E., Weller, A., & Lewis, R. (2012). Evaluation of geophysical techniques for dike inspection. *Journal of Environmental and Engineering Geophysics*, *17*(4), 185–195. https://doi.org/10.2113/JEEG17.4.185

Niemeyer, H. D., Eiben, H., & Rohde, H. (1996). History and heritage of German coastal engineering. In N. C. Kraus (Ed.), *History and heritage of coastal engineering* (pp. 169–213). American Society of Civil Engineers.

Nocedal, J., & Wright, S. (2006). *Numerical optimization*. Springer Science & Business Media.

Pageot, D., Le Feuvre, M., Leparoux, D., Côté, P., & Capdeville, Y. (2020). Assessment of physical properties of a sea dike using multichannel analysis of surface waves and 3D forward modeling. *Journal of Applied Geophysics*, *172*, 103841. https://doi.org/10.1016/j.jappgeo.2019.103841

Pan, Y., Gao, L., & Bohlen, T. (2018). Time-domain full-waveform inversion of Rayleigh and Love waves in presence of free-surface topography. *Journal of Applied Geophysics*, *152*, 77–85. https://doi.org/10.1016/j.jappgeo.2018.03.006

Podolski, C. (2015). Beitrag geophysikalischer Untersuchungen zur Rammschall-Prognose bei Gründung von Offshore-Bauwerken (Doctoral dissertation, Kiel University).

Rechtern, I. J. (2003). Standsicherheitsnachweise für Deichbauten. EFUC-Konferenz.

Richardson, M. D. (2002). Variability of shear wave speed and attenuation in surficial marine sediments. In *Impact of Littoral environmental variability of acoustic predictions and sonar performance* (pp. 107–114). Springer. https://doi.org/10.1007/978-94-010-0626-2_14

Rittgers, J. B., Revil, A., Planes, T., Mooney, M. A., & Koelewijn, A. R. (2015). 4-D imaging of seepage in earthen embankments with time-lapse inversion of self-potential data constrained by acoustic emissions localization. *Geophysical Journal International*, *200*(2), 758–772. https://doi.org/10.1093/gji/ggu432

Rusch, K., Köhn, D., Stümpel, H., Gauß, W., & Rabbel, W. (2022). Prehistoric chamber tombs or geological pitfall? A multimethod case study from Ancient Aigeira with a focus on seismic full-waveform inversion. *Archaeological Prospection*, *29*, 45–68. https://doi.org/10.1002/arp.1835

Sandmeier, K. J. (2004). Reflexw 3.5, http://www.sandmeier-geo.de/Download/reflexw_manual.pdf

Schön, J. (1983). *Petrophysik*. Ferdinand Enke Verlag.

Schön, J. H. (2015). *Physical properties of rocks: Fundamentals and principles of petrophysics*. Elsevier.

Schwardt, M., Köhn, D., Wunderlich, T., Wilken, D., Seeliger, M., Schmidts, T., Brückner, H., Başaran, S., & Rabbel, W. (2020). Characterization of silty to fine-sandy sediments with SH waves: Full waveform inversion in comparison with other geophysical methods. *Near Surface Geophysics*, *18*(3), 217–248. https://doi.org/10.1002/nsg.12097

Schwardt, M., Wilken, D., & Rabbel, W. (2021). Attenuation of seismic multiples in very shallow water: An application in archaeological prospection using data driven approaches. *Remote Sensing*, *13*(10), 1871. https://doi.org/10.3390/rs13101871

Stockwell, J. W. Jr. (1999). The CWP/SU: Seismic Un* x package. *Computers & Geosciences*, *25*(4), 415–419. https://doi.org/10.1016/S0098-3004(98)00145-9

Stolt, R. H. (1978). Migration by Fourier transform. *Geophysics*, *43*(1), 23–48. https://doi.org/10.1190/1.1440826

Ulugergerli, E. U., & Uyanik, O. (2007). Statistical correlations between seismic wave velocities and SPT blow counts and the relative density of soils. *Journal of Testing and Evaluation*, *35*(2), 187–191. https://doi.org/10.1520/JTE100159

Vidale, J. (1988). Finite-difference calculation of travel times. *Bulletin of the Seismological Society of America*, *78*(6), 2062–2076.

Virieux, J. (1984). SH-wave propagation in heterogeneous media: Velocity-stress finite-difference method. *Geophysics*, *49*(11), 1933–1942. https://doi.org/10.1190/1.1441605

Von Carnap-Bornheim, C., & Kalmring, S. (2011). DFG-Schwerpunktprogramm 1630 "Häfen von der Römischen Kaiserzeit bis zum Mittelalter. Zur Archäologie und Geschichte regionaler und überregionaler Verkehrssysteme". In B. V. Eriksen & I. Sonnenschein (Eds.), *Jahresbericht Zentrum für Baltische und Skandinavische Archäologie* (pp. 28–31). Schleswig, Germany: Stiftung Schleswig-Holsteinische Landesmuseen Schloss Gottorf.

Wilken, D., Hadler, H., Wunderlich, T., Majchczack, B., Schwardt, M., Fediuk, A., Fischer, P., Willerhäuser, T., Klooß, S., Vött, A., & Rabbel, W. (2022). Lost in the North Sea—Geophysical and geoarchaeological prospection of the Rungholt medieval dyke system (North Frisia, Germany). *PLoS ONE*, *17*(4), e0265463. https://doi.org/10.1371/journal.pone.0265463

Zeng, C., Xia, J., Miller, R. D., & Tsoflias, G. P. (2012). An improved vacuum formulation for 2D finite-difference modeling of Rayleigh waves including surface topography and internal discontinuities. *Geophysics*, *77*(1), T1–T9. https://doi.org/10.1190/geo2011-0067.1

How to cite this article: Schwardt, M., Wilken, D., Köhn, D., & Rabbel, W. (2023). A novel seismic full waveform inversion approach for assessing the internal structure of a medieval sea dike. *Archaeological Prospection*, *30*(4), 493–516. https://doi.org/10.1002/arp.1910

APPENDIX A: ADDITIONAL SHOT GATHERS FOR SELECTED SHOTS

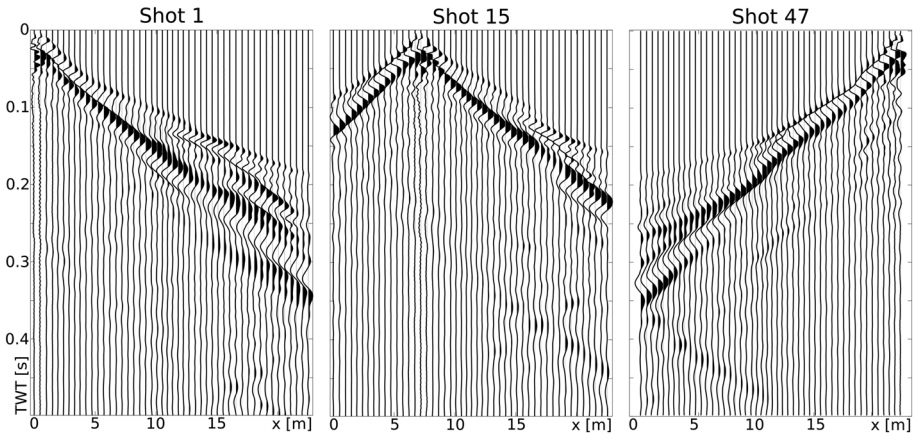

FIGURE A1 Raw data shot gather for three selected shots along the profile.

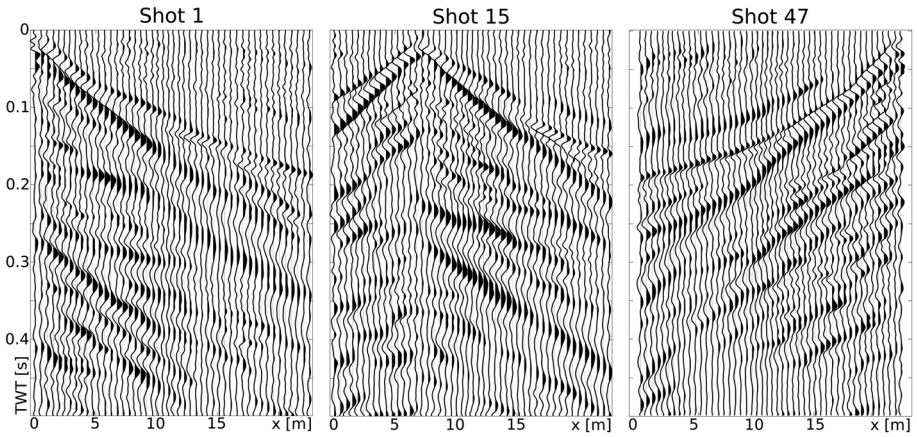

FIGURE A2 Processed shot gather for three selected shots along the profile. The data are spreading corrected and trace normalized. An f-k filter is used to suppress the dominant surface waves, followed by the application of a bandpass filter with cut-off frequencies of 10 and 100 Hz.

APPENDIX B: BASIC CONCEPT AND THEORY OF FWI

The FWI seeks to minimize the difference between calculated and measured data. Therefore, the core of the FWI approach is a precise computation of the seismic wavefield for a given subsurface model. The applied 2D-SH-FWI algorithm is based on the equations of motions for the propagation of Love and SH-waves in a 2D isotropic linear-visco-elastic medium. Assuming that Love and SH-wave propagation only have nonzero particle displacement in the *y*-direction perpendicular to the *x*-*z*-plane, the underlying forward problem can be expressed as:

$$\begin{aligned} \rho\frac{\partial v_y}{\partial t} &= \frac{\partial \sigma_{xy}}{\partial x} + \frac{\partial \sigma_{yz}}{\partial z} + f_y, \\ \frac{\partial \sigma_{xy}}{\partial t} &= \mu\left(\frac{\partial v_y}{\partial x}\right), \\ \frac{\partial \sigma_{yz}}{\partial t} &= \mu\left(\frac{\partial v_y}{\partial z}\right), \end{aligned} \tag{B1}$$

with v_y being the particle velocity component in y-direction, σ_{xy}, σ_{yz} the shear stresses and f_y the body force in y-direction. The core of the applied FWI algorithm is the numerical solution of Equation (B1), for which it needs to be discretized in space and time. This is done by a time-domain finite difference (FD) scheme with second-order operators in time and space on a staggered grid (Köhn et al., 2012; Levander, 1988; Virieux, 1984). At the bottom, left and right boundaries, the grid is surrounded by an absorbing frame of convolutional perfectly matched layers (C-PMLs; Komatitsch & Martin, 2007) to mitigate side as well as bottom reflections. At the top boundary, the free-surface condition $\sigma_{yz} = 0$ has to be satisfied to accurately account for Love-wave propagation. As the dike displays significant surface topography, this is realized by the improved vacuum formulation (Pan et al., 2018; Zeng et al., 2012). Viscoelastic effects on the dispersion of the Love and SH-wavefields are accounted for by a passive homogeneous Q_{SH} half-space model during forward and adjoint modelling by implementing a generalized standard linear solid composed of five relaxation mechanisms (Bohlen, 2002).

The minimization process of residuals between the field and modelled data is formulated as an iterative nonlinear optimization problem, for which an appropriate objective function E has to be defined. We use the trace normalized global correlation norm (GCN; after Choi & Alkhalifah, 2012), which previously has been applied successfully in other near-surface studies (e.g., Köhn et al., 2019; Rusch et al., 2022). It has been shown by e.g., Dokter et al. (2017) that the GCN has several advantages: The sensitivity with respect to amplitude errors is reduced and effects of varying amplitudes caused by e.g., insufficient receiver/source coupling are avoided to some extent, which is achieved by putting a stronger weight on the seismic phase information compared with the amplitude information. The GCN is given by

$$E = -\sum_{i=1}^{ns}\int_0^T dt \sum_{j=1}^{nr}\left[\frac{u_{ij}^{mod}(t)\,u_{ij}^{obs}(t)}{\left\|u_{ij}^{mod}(t)\right\|_2\left\|u_{ij}^{obs}(t)\right\|_2}\right], \tag{B2}$$

where ns and nr are the number of shots and receivers, respectively, T is the recording time of the seismic data, $\|\cdot\|_2$ denotes the L2-norm and u_{ij}^{mod} and u_{ij}^{obs} are the modelled and observed data, respectively. Minimizing the misfit between modelled and field data by means of this objective function is achieved by iteratively updating the model parameters m_n (here: v_{SH}, ρ) at each iteration step n using a gradient-based local optimization approach (Nocedal & Wright, 2006) starting with an initial model m_0 along a search direction δ_{mn} with a step length μ_n. For the computation of synthetic shots gathers, the unknown source wavelet is estimated during forward modelling by a linearly damped, least-squares optimization problem (Groos, 2013; Groos et al., 2014). We only use traces within an offset of maximum 2.5 m of the source for the inversion of the source wavelet. For further details regarding the applied FWI code, we refer to Köhn et al. (2014).

TABLE B1 Cut-off frequencies for the applied inversions steps.

Inversion steps	Lower cut-off frequency (Hz)	Upper cut-off frequency (Hz)
L-step	0	20–100
	Fixed	Increasing in steps of 20 Hz
B-step	20–80	100
	Increasing in steps of 20 Hz	Fixed
L-step	0	100
	Fixed	Fixed

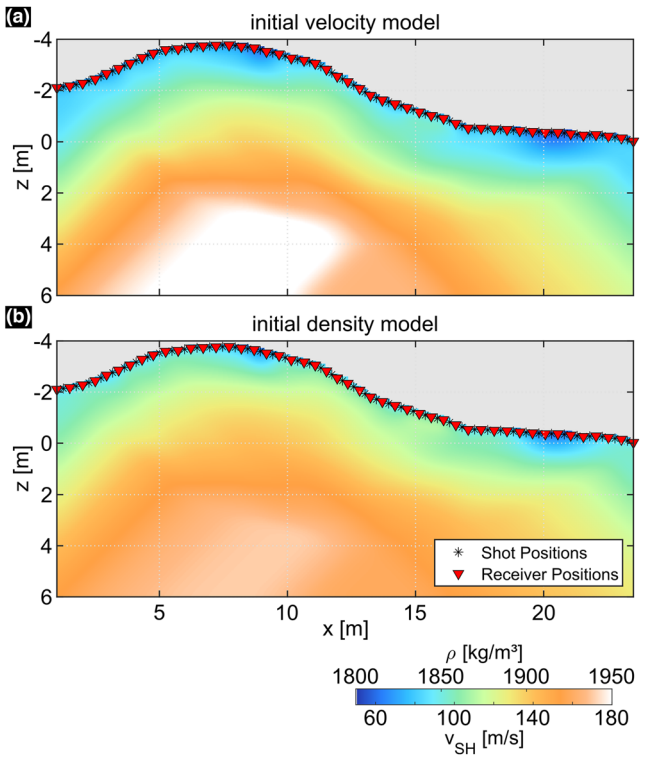

FIGURE B1 Initial velocity (a) and density (b) models for the FWI.

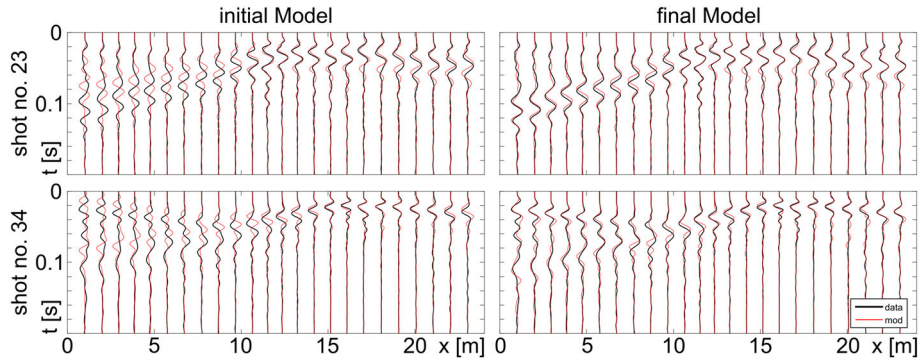

FIGURE B2 Comparison between measured (black) and modelled (red) data for the initial (left) and the final model (right) of the FWI, shown as zoom-in on the informative part of the waveforms (love-waves and refracted waves). The top row shows the comparison for shot gather with the worst fit (no. 23; $x = 10.73$ m), the bottom row for the best fitted shot gather (no. 34; $x = 15.81$ m). The data are trace normalized and bandpass filtered (10–100 Hz). For reasons of clarity, only every second trace is shown. The traces are aligned according to the approximate first arrival time of the first onsetting wave and are cut-off after 0.2 s after the first arrival.

APPENDIX C: ADDITIONAL INFORMATION FOR THE FATT

The initial shear-wave velocity model is based on the resulting velocity model of the first arrival travel time tomography (FATT), which has been applied to the data using the program Reflexw by Sandmeier Geo (Sandmeier, 2004). The algorithm, which is based on the Simultaneous Iterative Reconstruction Technique (SIRT; Dines & Lytle, 1979), calculates synthetic travel times using curved rays starting from the initial resp. current model, which are subsequently compared with the ones from the field data. For ray tracing, the method of Vidale (1988) is used, which is based on the FD-approximation of the eikonal equation. The model updates are derived from the resulting travel time residuals. This process is repeated until the maximum number of iterations is reached, or other pre-defined stopping criteria are met. For a detailed description of the theoretical framework, we refer the reader to (Sandmeier, 2004). In Reflexw, the initial model is defined by the minimum and maximum borders in x and z and a simple 1D gradient velocity model. The model is discretized on a 2D spatial Cartesian grid with 231 by 101 grid points and a grid spacing of 0.1 m in both x and z, which is smaller than half the average shot-receiver spacing. The velocity at the surface should be chosen within the expected range; here, it is estimated by the first arrival travel time picks for all shot-receiver pairs to be approximately 60 m/s. In Addition, a vertical velocity gradient (dv/dz) of 10 m/s/m is chosen. The model is limited to a maximum depth of 6 m, and the topography is accounted for by a minimum z-border of −4 m. The minimum and maximum expected velocities are set to 50 and 250 m/s, respectively. The smoothing values in x- and z-directions are both set to three grid points, equalling 0.3 m. An overview of the applied parameters is given in Table C1.

TABLE C1 Parameters applied during the first arrival travel time tomography and obtained differences after the final iteration.

Model depth (m)		Velocity range (m/s)		Velocity gradient (m/s/m)	Grid spacing (m)	Number of grid points (x by y)	Smoothing (grid points)
z_{min}	z_{max}	v_{min}	v_{max}				
−4	6	50	250	10	0.1	231 by 101	3

Iterations	Calculated rays	RMS deviation (ms)	Absolute time difference (s)	Total time difference (s)
19	2256	2.7	2.18	0.28

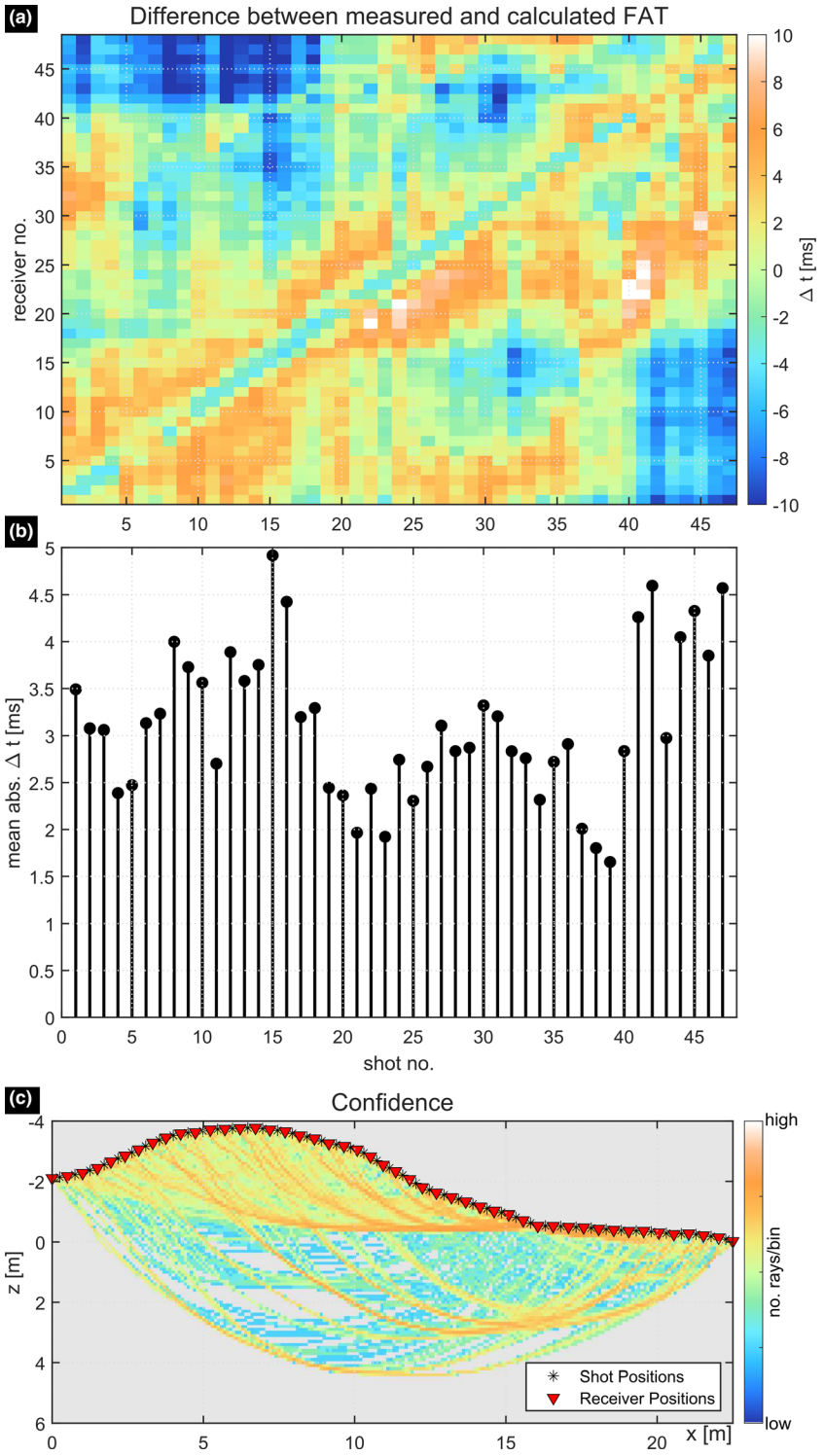

FIGURE C1 The time differences between all shot-receiver pairs (a) and the mean absolute time differences for each shot (b). (c) The confidence as ray coverage of the FATT model.

APPENDIX D: COMPARISONS BETWEEN THE DIFFERENT APPROACHES APPLIED DURING REFLECTION SEISMIC PROCESSING

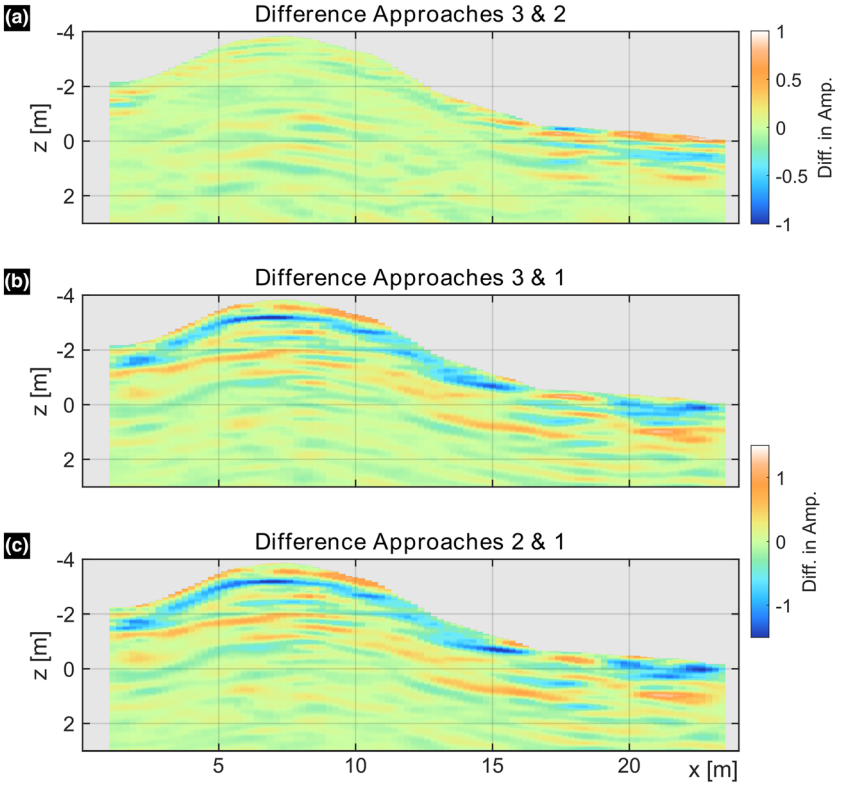

FIGURE D1 Differences between the final reflection seismic sections using the different approaches.

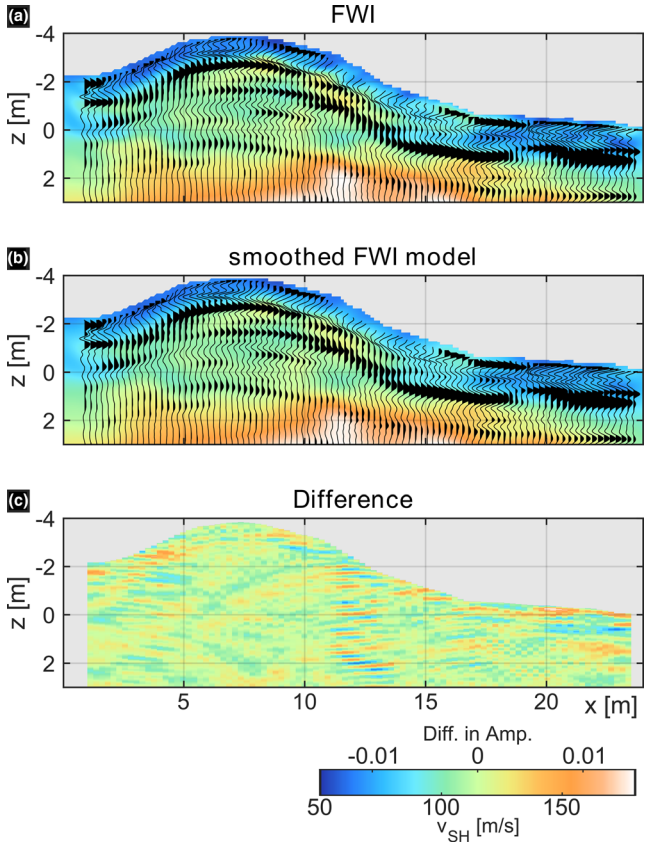

FIGURE D2 Comparison between the reflection seismic sections when applying the original (a) and a smoothed version (b) of the FWI velocity model for the reflection seismic processing. The reflection seismic sections are shown as wiggle traces on top of the FWI velocity model. (c) The differences between both final sections.

APPENDIX E: ADDITIONAL INFORMATION FOR THE REFLECTION SEISMIC SECTION

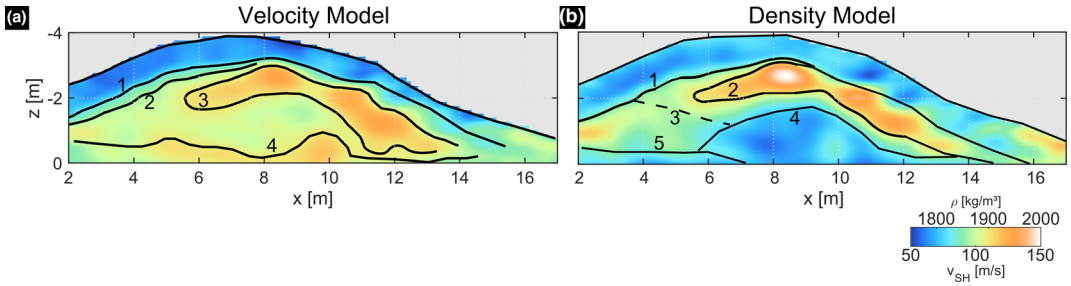

FIGURE E1 Isolines of the velocity (a) and density (b) model with their respective numbers.

TABLE E1 Isolines for the interpretational models.

Line number	Isoline v_{SH} (m/s)	Isoline ρ (kg/m^3)
1	70	1825
2	90	1900
3	110	1875
4	110	1825
5	-	1850

APPENDIX F: ADDITIONAL INFORMATION FOR THE REFLECTION SEISMIC SECTION

z (m below topography)	v_{SH} (m/s)	Mean wavelength λ_m (m)	Vertical resolution (m)
1	75	2.5	0.31–0.63
2	85	2.8	0.35–0.71
3	95	3.2	0.4–0.79
4	100	3.3	0.42–0.83
5	110	3.7	0.45–0.92
6	115	3.8	0.48–0.96
7.5	125	4.2	0.52–1.04
10	135	4.5	0.56–1.13

TABLE F1 Vertical resolution of the reflection seismic section for different depths, velocities and wavelengths for a central frequency of 30 Hz.